An alternative way to describe thermodynamically-consistent higher-order dissipation within strain gradient plasticity

Mohamed JEBAHI[a], Samuel FOREST[b]

[a]*Arts et Metiers Institute of Technology, CNRS, Université de Lorraine, LEM3, F-57000 Metz, France*
[b]*MINES Paris, PSL University, Centre des matériaux (CMAT), CNRS UMR 7633, BP 87, 91003 Evry, France*

Abstract

In the context of strain gradient plasticity (SGP), description of higher-order dissipation is the subject of extensive on-going discussions. In most existing SGP theories including thermodynamically-consistent higher-order dissipation, higher-order dissipative processes are described based on the decomposition of the higher-order stresses into recoverable and unrecoverable parts. This higher-order stress decomposition represents the basis of the so-called non-incremental (Gurtin-type) SGP theories, which are the most commonly used in the literature. As formulated, these theories satisfy the thermodynamic requirement of non-negative dissipation. However, they generally lead to unusual effects for some boundary value problems, such as the occurrence of elastic gaps under non-proportional loading conditions. The present work proposes an alternative way to describe higher-order dissipative effects, with an illustration within strain gradient crystal plasticity (SGCP) framework. Inspired by rheological models in series like Maxwell model, the higher-order stress decomposition is replaced by a decomposition of the plastic slip gradients into recoverable and unrecoverable parts. Effects of this decomposition technique are studied and compared with those obtained using higher-order stress decomposition. Capabilities of such a technique to deal with elastic gaps are also investigated.

Keywords: Strain gradient plasticity, crystal plasticity, size effects, internal length scales, higher-order recoverable effects, higher-order dissipative effects, elastic gaps

1. Introduction

Size effects in metals have been revealed by several small scale experiments (Fleck et al., 1994; Ma et al., 2012; Sarac et al., 2016; Dahlberg et al., 2017). More specifically, an increase in hardening and/or strengthening have been observed when deceasing the geometrical size in the size range between a few hundreds of nanometers and a few tens of micrometers. These effects can be explained by the so-called geometrically necessary dislocations (GNDs) which are associated with nonuniform plastic straining (Ashby, 1970). To overcome limitations of conventional plasticity theories in capturing such effects, Aifantis (1984, 1987) has proposed in a pioneering work a strain gradient plasticity (SGP) theory, in which a plastic strain gradient term is added to the conventional yield function. Motivated by the interesting features of this theory, numerous SGP models have been developed over the last three decades for both single- and polycrystal structures. Both lower- and higher-order SGP models can be found in the literature. Lower-order models preserve the structure of classical plasticity (with conventional stresses, equilibrium equations and boundary conditions), with the difference that the yield condition includes strain gradient terms (Aifantis,

Email addresses: mohamed.jebahi@ensam.eu (Mohamed JEBAHI), samuel.forest@minesparis.psl.eu (Samuel FOREST)

1984; Mühlhaus and Alfantis, 1991; Acharya and Bassani, 2000). Although offering a simplified modeling framework, these models can yield likely unacceptable behaviors with pathological mesh dependence for some problems (Niordson and Hutchinson, 2003). Higher-order SGP approaches substantially deviate from conventional plasticity by considering new higher-order stresses and additional equilibrium and boundary conditions (Fleck and Hutchinson, 1997; Aifantis, 1999; Gurtin, 2002, 2004; Gurtin et al., 2007; Forest and Aifantis, 2010; Bardella, 2010; Forest and Bertram, 2011; Anand et al., 2012; Cordero et al., 2016; Forest, 2020; El-Naaman et al., 2019; Jebahi et al., 2020; Jebahi and Forest, 2021; Cai et al., 2021). It is nowadays widely accepted that higher-order SGP theories offer powerful modeling capabilities, making them the most commonly used in the literature.

One of the challenging issues related to higher-order SGP theories is how to calculate the additional higher-order stresses. Inspired by conventional plasticity, in the early higher-order SGP theories, these stresses are calculated incrementally based on the increments of the plastic gradients. As an example of such theories, which are known as incremental theories, the approach proposed by Fleck and Hutchinson (2001) as a generalization of the J_2 flow theory can be cited. This approach represents the basis of incremental theories. However, as pointed out by Gudmundson (2004) and Gurtin and Anand (2009), it does not always satisfy the thermodynamic requirement of non-negative dissipation, unless the nonlocal terms are dropped. A modified version of this theory in which the higher-order stresses are assumed to be fully recoverable is proposed by Hutchinson (2012) to ensure its thermodynamic consistency. Although used in subsequent works to develop thermodynamically-acceptable incremental models (Fleck et al., 2014, 2015; Nellemann et al., 2017, 2018), the assumption of no higher-order contribution to dissipation does not seem to rely on physical arguments. Its consistency with the current understanding of dislocation mechanics is questioned (Fleck and Willis, 2009; Voyiadjis and Deliktas, 2009). As reported by Fleck and Willis (2009), direct experimental measurement shows that the core energy of dislocations stored during plastic deformation is much smaller than the plastic work dissipated in dislocation motion. Consequently, both statistically stored dislocations (SSDs) and geometrically necessary dislocations (GNDs) would contribute more to plastic dissipation than to a change in the free energy. Until now, there exist no thermodynamically-acceptable recipes for an incremental model capable of modeling higher-order dissipative effects (Fleck et al., 2015).

To overcome limitations of incremental SGP theories in modeling thermodynamically-consistent higher-order dissipation, non-incremental (Gurtin-type) approaches have been developed (Gurtin, 2004; Gurtin et al., 2007). In these approaches, the higher-order stresses are decomposed into recoverable (also called energetic) and unrecoverable (also called dissipative) parts. To satisfy the requirement of non-negative dissipation, the dissipative (unrecoverable) higher-order stresses are directly expressed in terms of increments of the plastic gradients. Thanks to their interesting features, Gurtin-type SGP models have received a lot of attention in recent years, and numerous variations of such models have been developed for single- and poly-crystal structures (Gurtin, 2008; Gurtin and Anand, 2009; Bardella and Panteghini, 2015; Wulfinghoff et al., 2015; Wulfinghoff and Böhlke, 2015; Panteghini and Bardella, 2018; Martínez-Pañeda et al., 2019; Jebahi et al., 2020; Cai et al., 2021). An overview of key Gurtin-type theories can be found in Voyiadjis and Song (2019, 2020). As formulated, such theories allow for considering thermodynamically-consistent higher-order dissipation. However, they may lead to unusual phenomena under certain conditions, like the occurrence of elastic gaps under non-proportional loading conditions (Hutchinson, 2012; Fleck et al., 2014, 2015). As pointed out by Fleck et al. (2015), non-incremental theories including higher-order dissipation always generate elastic gaps for some boundary value problems. The existence of such gaps in reality is often questioned, as they reflect a finite change in the higher-order stresses after an infinitesimal change in the plastic strain gradients.

In the absence of experimental works studying the physical nature of elastic gaps, next generation of gradient-enhanced models allowing for removing such gaps while including thermodynamically-consistent higher-order dissipation would be very useful. In this context, Panteghini et al. (2019) have recently proposed a phenomenological SGP model based on a particular definition of the free energy density as a sum of elementary quadratic plastic strain gradient functions that become linear at different threshold values. This

model has been applied by Panteghini and Bardella (2020) to simulate the cyclic response of poly-crystal micro-sized copper wires. Good results have been obtained which compare favorably with the experimental results of Liu et al. (2013). However, a large number of elementary quadratic functions are generally required to obtain satisfactory results. To simplify identification of the associated parameters, a robust calibration procedure has been proposed by the authors (Panteghini et al., 2019; Panteghini and Bardella, 2020). Using an original multiple kinematic decomposition of the Nye's tensor (Nye, 1953) into recoverable and recoverable parts, the phenomenological model of Panteghini et al. (2019) is the only existing gap-free model that is capable of reproducing thermodynamically-consistent higher-order dissipation (Panteghini et al., 2019; Bardella, 2021). It is worth mentioning that kinematic decomposition techniques have already been discussed in several works on generalized continua, including Cosserat (de Borst, 1993; Forest et al., 1997; Forest and Sievert, 2003), micromorphic (Forest and Sievert, 2003; Forest, 2009; Regueiro, 2010) and strain gradient (Gologanu et al., 1997; Fleck and Hutchinson, 1997) continua. In the context of strain gradient plasticity, this kind of decomposition has only been discussed using phenomenological theories (Forest and Sievert, 2003; Forest, 2020; Panteghini et al., 2019). To the best of the authors knowledge, no application to SGCP exists in the literature. In the present work, an alternative application of this kind of decomposition is proposed to describe recoverable and unrecoverable higher-order effects, with an illustration within SGCP framework. As a generalization of the displacement gradient decomposition, which is widely used in conventional small deformation plasticity, the higher-order stress decomposition classically used in Gurtin-type models is replaced by a decomposition of the plastic slip gradients into recoverable (non-dissipative) and unrecoverable (dissipative) parts. An in-depth investigation of the proposed kinematic decomposition and its effects on the response of single-crystal materials is conducted in this paper. As will be seen later, the developed SGCP model based on this decomposition represents the first gradient-enhanced single-crystal model that includes higher-order dissipation and systematically avoids elastic gaps.

After the present introduction, the present paper is organized as follows. Section 2 presents the main features of the proposed SGCP model, based on the decomposition of the plastic slip gradients into recoverable and unrecoverable parts. This model is developed assuming generalized non-quadratic defect energy and uncoupled dissipation. Section 3 discusses the implementation of a simplified two-dimensional (2D) version of the proposed SGCP model. This version is used to investigate, in a simple manner, the effects of the implied dissipative constitutive parameters on the global response of a crystalline strip subjected to proportional and non-proportional shear loading conditions. Results of this investigation are presented in Section 4. A comparison with the Gurtin-type SGCP model of Jebahi et al. (2020), which is based on classical higher-order stress decomposition, is also given in Section 4. Finally, Section 5 presents some concluding remarks.

2. Strain gradient crystal plasticity (SGCP) model based on plastic slip gradient decomposition

2.1. Single crystal kinematics

Let $\mathbf{u}(\mathbf{x}, t)$ denotes the displacement at time t of an arbitrary material point identified by $\mathbf{x}$ in a subregion $\mathcal{V}$ of the studied continuum. Within small deformation framework, the displacement gradient $\boldsymbol{\nabla}\mathbf{u}$ can be additively decomposed as follows:

$$\boldsymbol{\nabla}\mathbf{u} = \mathbf{H}_e + \mathbf{H}_p \tag{1}$$

where $\mathbf{H}_e$ and $\mathbf{H}_p$ represents respectively the elastic distortion, due to stretch and rotation of the underlying lattice, and the plastic distortion, due to plastic flow. Their symmetric parts define the elastic and plastic strain tensors, and their skew-symmetric parts give the elastic and plastic rotation tensors:

$$\boldsymbol{\varepsilon}_e = \frac{1}{2}\left[\mathbf{H}_e + \mathbf{H}_e^T\right],\ \boldsymbol{\varepsilon}_p = \frac{1}{2}\left[\mathbf{H}_p + \mathbf{H}_p^T\right],\ \boldsymbol{\omega}_e = \frac{1}{2}\left[\mathbf{H}_e - \mathbf{H}_e^T\right],\ \boldsymbol{\omega}_p = \frac{1}{2}\left[\mathbf{H}_p - \mathbf{H}_p^T\right] \tag{2}$$

In single-crystal plasticity, the plastic distortion rate tensor can be expressed as:

$$\dot{\mathbf{H}}_p = \sum_{\alpha=1}^{q} \dot{\gamma}^\alpha \left[\mathbf{s}^\alpha \otimes \mathbf{m}^\alpha\right] \tag{3}$$

where $\dot{\gamma}^\alpha$, $\mathbf{s}^\alpha$ and $\mathbf{m}^\alpha$ are respectively the plastic slip rate, the unit slip direction and the unit slip-plane normal associated with slip system α, q is the total number of slip systems, and "$\otimes$" is the tensor product operator. Therefore, the plastic strain rate tensor $\dot{\boldsymbol{\varepsilon}}_p$ can be written as:

$$\dot{\boldsymbol{\varepsilon}}_p = \sum_{\alpha=1}^{q} \dot{\gamma}^\alpha \mathbf{P}^\alpha \tag{4}$$

with $\mathbf{P}^\alpha$ the symmetrized Schmid tensor associated with slip system α:

$$\mathbf{P}^\alpha = \frac{1}{2}\left(\mathbf{s}^\alpha \otimes \mathbf{m}^\alpha + \mathbf{m}^\alpha \otimes \mathbf{s}^\alpha\right) \tag{5}$$

2.2. Balance equations

In the considered gradient-enhanced continuum, both displacement and plastic slip fields are considered as primary variables. Therefore, application of the principle of virtual power (Germain, 1973; Forest and Aifantis, 2010; Forest and Bertram, 2011) leads to two kinds of balance equations. Assuming static case with no body forces, the macroscopic balance equations and the associated boundary conditions can be expressed as (Gurtin et al., 2007):

$$\left\{\begin{array}{rcll} \boldsymbol{\nabla}\cdot\boldsymbol{\sigma} & = & \mathbf{0} & \text{in} \quad \mathcal{V} \\ \boldsymbol{\sigma}\cdot\mathbf{n} & = & \mathbf{t} & \text{on} \quad \mathcal{S} \end{array}\right. \tag{6}$$

where $\boldsymbol{\sigma}$ represents the classical macroscopic Cauchy stress tensor, $\mathbf{t}$ is the macroscopic traction force acting on the boundary $\mathcal{S}$ of the considered subregion $\mathcal{V}$, and $\mathbf{n}$ is the outward unit normal to $\mathcal{S}$. The microscopic counterparts can be obtained as (Gurtin et al., 2007):

$$\left\{\begin{array}{rcll} \tau^\alpha + \boldsymbol{\nabla}\cdot\boldsymbol{\xi}^\alpha - \pi^\alpha & = & 0 & \text{in} \quad \mathcal{V} \\ \boldsymbol{\xi}^\alpha\cdot\mathbf{n} & = & \chi^\alpha & \text{on} \quad \mathcal{S} \end{array}\right. \tag{7}$$

where τ^α is the resolved shear stress on slip system α, π^α is a microscopic stress scalar defined on slip system α (work-conjugate to γ^α), $\boldsymbol{\xi}^\alpha$ is a microscopic stress vector defined on slip system α (work-conjugate to $\boldsymbol{\nabla}\gamma^\alpha$), χ^α is a microscopic traction force for slip system α acting on $\mathcal{S}$. In what follows, the symbol $\boldsymbol{\kappa}^\alpha$ is used to denote the plastic slip gradient associated with slip system α ($\boldsymbol{\kappa}^\alpha = \boldsymbol{\nabla}\gamma^\alpha$).

2.3. Basis of the proposed SGCP model: comparison with classical Gurtin-type SGCP models

The present subsection details the general theoretical formulation of the proposed SGCP model, based on the decomposition of the plastic slip gradients into recoverable and unrecoverable parts. For comparison purposes, the main features of classical Gurtin-type SGCP models (Gurtin et al., 2007, 2010; Yalçinkaya, 2016; Jebahi et al., 2020) are first reviewed. As in the latter models, the power density of internal forces in the present one is given by:

$$p_{int} = \boldsymbol{\sigma} : \dot{\boldsymbol{\varepsilon}}_e + \sum_{\alpha=1}^{q} \pi^\alpha \dot{\gamma}^\alpha + \sum_{\alpha=1}^{q} \boldsymbol{\xi}^\alpha \cdot \dot{\boldsymbol{\kappa}}^\alpha \tag{8}$$

and the dissipation inequality (also called free energy imbalance or simply entropy imbalance) can be written in local form as:

$$p_{int} - \dot{\psi} \geq 0 \tag{9}$$

with ψ the Helmholtz free energy volume density. Differences between the present and classical Gurtin-type SGCP models lie in the definition and arguments of this density.

2.3.1. Classical Gurtin-type SGCP models

The free energy density involved in classical Gurtin-type SGCP models is generally assumed to be a function of the elastic strain tensor, the plastic slips and their gradients (Gurtin et al., 2007, 2010; Yalçinkaya, 2016; Jebahi et al., 2020):

$$\psi = \psi\left(\boldsymbol{\varepsilon}_e,\, \boldsymbol{\gamma},\, \boldsymbol{\kappa}\right) \tag{10}$$

with $\boldsymbol{\gamma} = \left(\gamma^1,\, \gamma^2,\, ...,\, \gamma^q\right)$ and $\boldsymbol{\kappa} = \left(\boldsymbol{\kappa}^1,\, \boldsymbol{\kappa}^2,\, ...,\, \boldsymbol{\kappa}^q\right)$ the vectors of the plastic slips and their gradients. Using this expression, the dissipation inequality (9) can be written in a more explicit form as:

$$\left(\boldsymbol{\sigma} - \frac{\partial \psi}{\partial \boldsymbol{\varepsilon}_e}\right) : \dot{\boldsymbol{\varepsilon}}_e + \sum_{\alpha=1}^{q} \left(\pi^\alpha - \frac{\partial \psi}{\partial \gamma^\alpha}\right) \dot{\gamma}^\alpha + \sum_{\alpha=1}^{q} \left(\boldsymbol{\xi}^\alpha - \frac{\partial \psi}{\partial \boldsymbol{\kappa}^\alpha}\right) \cdot \dot{\boldsymbol{\kappa}}^\alpha \geq 0 \tag{11}$$

The macroscopic stress $\boldsymbol{\sigma}$ is generally assumed to be recoverable:

$$\boldsymbol{\sigma} = \frac{\partial \psi}{\partial \boldsymbol{\varepsilon}_e} \tag{12}$$

and the microscopic stresses can be divided into recoverable and unrecoverable (dissipative) parts:

$$\pi^\alpha = \pi^\alpha_r + \pi^\alpha_d \quad \text{and} \quad \boldsymbol{\xi}^\alpha = \boldsymbol{\xi}^\alpha_r + \boldsymbol{\xi}^\alpha_d \tag{13}$$

with the recoverable parts determined as:

$$\pi^\alpha_r = \frac{\partial \psi}{\partial \gamma^\alpha} \quad \text{and} \quad \boldsymbol{\xi}^\alpha_r = \frac{\partial \psi}{\partial \boldsymbol{\kappa}^\alpha} \tag{14}$$

The residual dissipation can then be written as:

$$\sum_{\alpha=1}^{q} \pi^\alpha_d \, \dot{\gamma}^\alpha + \sum_{\alpha=1}^{q} \boldsymbol{\xi}^\alpha_d \cdot \dot{\boldsymbol{\kappa}}^\alpha \geq 0 \tag{15}$$

Note that $\boldsymbol{\xi}^\alpha_d$, which characterizes the dissipative microscopic forces associated with the motion of dislocations within the slip plane α, is required to be tangent to this plane. Therefore, the plastic slip gradient rate $\dot{\boldsymbol{\kappa}}^\alpha$ in the above inequality can be replaced, without loss in generality, by its corresponding tangential gradient rate defined by:

$$\dot{\boldsymbol{\kappa}}^{\alpha t} = \left(\mathbf{s}^\alpha \cdot \dot{\boldsymbol{\kappa}}^\alpha\right) \mathbf{s}^\alpha + \left(\mathbf{l}^\alpha \cdot \dot{\boldsymbol{\kappa}}^\alpha\right) \mathbf{l}^\alpha \tag{16}$$

where $\mathbf{l}^\alpha = \mathbf{m}^\alpha \times \mathbf{s}^\alpha$ represents the line direction of the dislocation distribution in slip system α, and "$\times$" denotes the cross product operator. To satisfy (15), π^α_d and $\boldsymbol{\xi}^\alpha_d$ can be described using simple rate-dependent constitutive relations in the form:

$$\pi^\alpha_d = S^\alpha \, R\left(\dot{e}^\alpha\right) \frac{\dot{\gamma}^\alpha}{\dot{e}^\alpha} \quad \text{and} \quad \boldsymbol{\xi}^\alpha_d = S^\alpha \, R\left(\dot{e}^\alpha\right) \frac{\dot{\boldsymbol{\kappa}}^{\alpha t}}{\dot{e}^\alpha} \tag{17}$$

where S^α is a strictly positive stress-dimensional internal state variable characterizing the dissipative slip resistance on slip system α, R is a rate-sensitivity function, and $\dot{e}^\alpha$ is an effective plastic slip rate measure calculated based on the plastic slip and plastic slip gradient rates associated with slip system α. To provide more flexibility in controlling first- and higher-order dissipative processes, two independent effective plastic slip rate measures are used in Jebahi et al. (2020) to calculate π^α_d and $\boldsymbol{\xi}^\alpha_d$ (the first- and higher-order dissipative effects are assumed to be uncoupled). The above forms of π^α_d and $\boldsymbol{\xi}^\alpha_d$ tacitly assume zero activation stress

for initiation of inelastic deformation. This makes it possible to avoid numerical issues related to the identification and treatment of activated slip systems. As done in some works (Yalçinkaya, 2016; Jebahi et al., 2020), π_d^α and $\boldsymbol{\xi}_d^\alpha$ can also be determined based on dissipation pseudo-potentials. To ensure the requirement of non-negative dissipation, it is sufficient that these pseudo-potentials are non-negative and convex in $\dot{\gamma}^\alpha$ and $\dot{\boldsymbol{\kappa}}^\alpha$ (Šilhavý, 1997).

As formulated, classical Gurtin-type SGCP models Gurtin et al. (2007) satisfy the requirement of non-negative dissipation. However, they generally lead to unusual phenomena under certain conditions, like the occurrence of elastic gaps under non-proportional loading conditions (Hutchinson, 2012; Fleck et al., 2014, 2015). For more details about these models, the reader is referred to the original paper of Gurtin et al. (2007).

2.3.2. Proposed SGCP model

As a generalization of the displacement gradient decomposition (1), which is widely used in conventional small deformation plasticity, the higher-order stress decomposition used in classical Gurtin-type SGCP models is replaced by a decomposition of the plastic slip gradients $\boldsymbol{\kappa}^\alpha$ into recoverable (non-dissipative) $\boldsymbol{\kappa}_r^\alpha$ and unrecoverable (dissipative) $\boldsymbol{\kappa}_d^\alpha$ parts:

$$\boldsymbol{\kappa}^\alpha = \boldsymbol{\kappa}_r^\alpha + \boldsymbol{\kappa}_d^\alpha \tag{18}$$

Compared to the model of Panteghini et al. (2019), which is based on multiple decomposition of the primal kinematic higher-order fields, only one decomposition is applied to each slip system. This decomposition implies the existence of a similar decomposition for the GND densities, which are given by (Arsenlis and Parks, 1999):

$$\rho_{\vdash}^\alpha = -\mathbf{s}^\alpha \cdot \boldsymbol{\kappa}^\alpha \quad \text{and} \quad \rho_{\odot}^\alpha = \mathbf{l}^\alpha \cdot \boldsymbol{\kappa}^\alpha \tag{19}$$

where $\rho_{\vdash}^\alpha$ and $\rho_{\odot}^\alpha$ are edge and screw dislocation densities associated with slip system α. Considering (18), these densities can be split into recoverable and unrecoverable parts:

$$\begin{cases} \rho_{\vdash}^\alpha = \varrho_{\vdash}^\alpha + \eta_{\vdash}^\alpha \quad \text{with} \quad \varrho_{\vdash}^\alpha = -\mathbf{s}^\alpha \cdot \boldsymbol{\kappa}_r^\alpha \quad \text{and} \quad \eta_{\vdash}^\alpha = -\mathbf{s}^\alpha \cdot \boldsymbol{\kappa}_d^\alpha \\ \rho_{\odot}^\alpha = \varrho_{\odot}^\alpha + \eta_{\odot}^\alpha \quad \text{with} \quad \varrho_{\odot}^\alpha = \mathbf{l}^\alpha \cdot \boldsymbol{\kappa}_r^\alpha, \quad \text{and} \quad \eta_{\odot}^\alpha = \mathbf{l}^\alpha \cdot \boldsymbol{\kappa}_d^\alpha \end{cases} \tag{20}$$

Unlike in classical Gurtin-type SGCP models, only the recoverable parts of the plastic slip gradients, or equivalently the recoverable parts of the GND densities, are involved in the definition of the free energy density associated with the present model:

$$\psi = \psi\left(\boldsymbol{\varepsilon}_e,\, \boldsymbol{\gamma},\, \boldsymbol{\kappa}_r\right) \tag{21}$$

where $\boldsymbol{\kappa}_r = \left(\boldsymbol{\kappa}_r^1,\, \boldsymbol{\kappa}_r^2,\, ...,\, \boldsymbol{\kappa}_r^q\right)$ denotes the vector of all the recoverable parts of the plastic slip gradients. Using this definition, the dissipation inequality (9) becomes:

$$\left(\boldsymbol{\sigma} - \frac{\partial \psi}{\partial \boldsymbol{\varepsilon}_e}\right) : \dot{\boldsymbol{\varepsilon}}_e + \sum_{\alpha=1}^{q} \left(\pi^\alpha - \frac{\partial \psi}{\partial \gamma^\alpha}\right) \dot{\gamma}^\alpha + \sum_{\alpha=1}^{q} \left(\boldsymbol{\xi}^\alpha - \frac{\partial \psi}{\partial \boldsymbol{\kappa}_r^\alpha}\right) \cdot \dot{\boldsymbol{\kappa}}_r^\alpha + \sum_{\alpha=1}^{q} \boldsymbol{\xi}^\alpha \cdot \dot{\boldsymbol{\kappa}}_d^\alpha \geq 0 \tag{22}$$

As in classical Gurtin-type SGCP models, the macroscopic stress $\boldsymbol{\sigma}$ is assumed to be recoverable:

$$\boldsymbol{\sigma} = \frac{\partial \psi}{\partial \boldsymbol{\varepsilon}_e} \tag{23}$$

and the first-order microscopic stresses can be divided into recoverable and dissipative parts:

$$\pi^\alpha = \pi_r^\alpha + \pi_d^\alpha \tag{24}$$

with the recoverable parts given by:

$$\pi_r^\alpha = \frac{\partial \psi}{\partial \gamma^\alpha} \tag{25}$$

In the present model, the higher-order dissipation is modeled through the dissipative parts of the plastic slip gradients. Therefore, unlike classical Gurtin-type SGCP models, the higher-order microscopic stresses are considered as recoverable:

$$\boldsymbol{\xi}^\alpha = \frac{\partial \psi}{\partial \boldsymbol{\kappa}_r^\alpha} \tag{26}$$

Using the above constitutive assumptions, the residual dissipation becomes:

$$\sum_{\alpha=1}^{q} \pi_d^\alpha \, \dot{\gamma}^\alpha + \sum_{\alpha=1}^{q} \boldsymbol{\xi}^\alpha \cdot \dot{\boldsymbol{\kappa}}_d^\alpha \geq 0 \tag{27}$$

Here, the higher-order dissipation is given by $\boldsymbol{\xi}^\alpha \cdot \dot{\boldsymbol{\kappa}}_d^\alpha$ instead of $\boldsymbol{\xi}_d^\alpha \cdot \dot{\boldsymbol{\kappa}}^\alpha$ in the dissipation inequality (15) associated with classical Gurtin-type SGCP models. As in the latter models, tangential higher-order stresses are considered in this work (*i.e.,* $\boldsymbol{\xi}^\alpha$ is considered to be tangent to the slip plane α, for any α). Following Jebahi et al. (2020), first- and higher-order dissipative effects are assumed to be uncoupled and described using independent effective plastic slip measures. By doing so, the two terms of the above residual dissipation (27) can be treated separately. To ensure non-negative first-order dissipation ($\pi_d^\alpha \, \dot{\gamma}^\alpha \geq 0$), the first-order dissipative stresses can simply be described using rate-dependent constitutive laws similar to those used in conventional CP:

$$\pi_d^\alpha = S_\pi^\alpha \, R\left(\dot{e}_\pi^\alpha\right) \frac{\dot{\gamma}^\alpha}{\dot{e}_\pi^\alpha} \quad \text{with} \quad \dot{e}_\pi^\alpha = |\dot{\gamma}^\alpha| \tag{28}$$

where $S_\pi^\alpha > 0$ is a stress-dimensional slip resistance associated with slip system α. This variable is referred to hereafter as first-order slip resistance. Concerning the higher-order dissipation, special treatment is required as no higher-order dissipative stresses are explicitly considered. In this work, the higher-order dissipation is accounted for by constraining the evolution of the recoverable higher-order stresses. Within rate-independent framework, this can be done by assuming the existence of higher-order yield functions defined in the higher-order stress space as:

$$f^\alpha = \xi_{eq}^\alpha - S_\xi^\alpha \, l_d \tag{29}$$

where $S_\xi^\alpha \geq 0$ is a stress-dimensional slip resistance associated with slip system α, referred to hereafter as higher-order dissipative slip resistance, l_d is a dissipative length scale, and ξ_{eq}^α is the equivalent higher-order stress associated with slip system α, defined by (note that $\boldsymbol{\xi}^\alpha$ is tangent to the slip plane α):

$$\xi_{eq}^\alpha = \sqrt{\left(\mathbf{s}^\alpha \cdot \boldsymbol{\xi}^\alpha\right)^2 + \left(\mathbf{l}^\alpha \cdot \boldsymbol{\xi}^\alpha\right)^2} = \|\boldsymbol{\xi}^\alpha\| \tag{30}$$

Non-negative higher-order dissipation ($\boldsymbol{\xi}^\alpha \cdot \dot{\boldsymbol{\kappa}}_d^\alpha \geq 0$) can be satisfied by assuming normality-like flow rules for $\dot{\boldsymbol{\kappa}}_d^\alpha$:

$$\dot{\boldsymbol{\kappa}}_d^\alpha = \frac{\dot{\kappa}_d^\alpha}{l_d} \frac{\partial f^\alpha}{\partial \boldsymbol{\xi}^\alpha} = \frac{\dot{\kappa}_d^\alpha}{l_d} \frac{\boldsymbol{\xi}^\alpha}{\xi_{eq}^\alpha} \quad \text{with} \quad \dot{\kappa}_d^\alpha = \|l_d \, \dot{\boldsymbol{\kappa}}_d^\alpha\| \tag{31}$$

It can verified that $\dot{\boldsymbol{\kappa}}_d^\alpha$ is also tangent to the slip plane α. Using this rate-independent framework, special techniques are required to deal with numerical issues related to the identification and treatment of the higher-order activated slip systems ($i.e.$, systems for which the higher-order yield condition is fulfilled). To avoid

these issues, the higher-order yield functions can be replaced by simple rate-dependent constitutive equations for ξ^{α}_{eq} in the form:

$$\xi^{\alpha}_{eq} = S^{\alpha}_{\xi}\, l_d\, R\left(\dot{\kappa}^{\alpha}_{d}\right) \qquad \text{with} \qquad \dot{\boldsymbol{\kappa}}^{\alpha}_{d} = \frac{\dot{\kappa}^{\alpha}_{d}}{l_d}\,\frac{\boldsymbol{\xi}^{\alpha}}{\xi^{\alpha}_{eq}}$$

This option is adopted in the present work to model the higher-order dissipation. It should be noted that the description of the higher-order dissipation within the higher-order stress space (*i.e.,* by constraining the evolution of the higher-order stresses) is different from that proposed in Panteghini et al. (2019) which is given in the higher-order strain space (*i.e.,* by constraining the evolution of the primal kinematic higher-order fields). The description proposed in the present work allows for considering more naturally dissipative (isotropic-like) higher-order hardening as in conventional plasticity theories.

2.4. Constitutive laws

In the previous subsection, the theoretical formulation of the proposed SGCP model is discussed using general form of the free energy density. The present subsection aims at deriving specific constitutive laws for the macroscopic and microscopic stresses involved in the balance equations [$(6)_1$ and $(7)_1$], assuming a particular form of the free energy density close to that used in Jebahi et al. (2020).

2.4.1. Constitutive laws for the recoverable stresses

Inspired by Jebahi et al. (2020), the free energy density ψ adopted in this work is assumed to be the sum of a quadratic elastic energy density ψ_e, only depending on $\boldsymbol{\varepsilon}_e$, and a power-law defect energy density ψ_p, only depending on the recoverable parts of the GND densities:

$$\begin{aligned} \psi\left(\boldsymbol{\varepsilon}_e,\, \boldsymbol{\varrho}^{\boldsymbol{\alpha}}\right) &= \psi_e\left(\boldsymbol{\varepsilon}_e\right) &+ \psi_p\left(\boldsymbol{\varrho}^{\boldsymbol{\alpha}}\right) \\ &= \tfrac{1}{2}\,\boldsymbol{\varepsilon}_e : \mathbf{C} : \boldsymbol{\varepsilon}_e &+ \frac{1}{n}\, X_0\, l^n_{en} \sum_{\alpha=1}^{q} \left[\left|\varrho^{\alpha}_{\vdash}\right|^n + \left|\varrho^{\alpha}_{\odot}\right|^n\right] \end{aligned} \tag{32}$$

where $\mathbf{C}$ is symmetric positive-definite elasticity tensor, X_0 is a constant representing the higher-order non-dissipative (energetic) slip resistance, l_{en} is a non-dissipative (energetic) length scale, and n is an adjustable order-controlling index ($n \geq 1$). The adopted power-law form of the defect energy density has been used in several gradient-based works (Bayerschen and Böhlke, 2016; Panteghini et al., 2019). The special case of $n = 1$ corresponds to the case of non-interacting dislocations with a defect energy density being linear in the dislocation densities (Ohno and Okumura, 2007; Wulfinghoff et al., 2015). Considering (20), the above expression of ψ can be rewritten, in a more convenient form, as follows:

$$\psi\left(\boldsymbol{\varepsilon}_e,\, \boldsymbol{\kappa}_r\right) = \frac{1}{2}\,\boldsymbol{\varepsilon}_e : \mathbf{C} : \boldsymbol{\varepsilon}_e + \frac{1}{n}\, X_0\, l^n_{en} \sum_{\alpha=1}^{q} \left[\left|\mathbf{s}^{\alpha} \cdot \boldsymbol{\kappa}^{\alpha}_r\right|^n + \left|\mathbf{l}^{\alpha} \cdot \boldsymbol{\kappa}^{\alpha}_r\right|^n\right] \tag{33}$$

Using this expression, the state laws given by (23), (25) and (26) can be expressed as (see Appendix A):

$$\left\{\begin{array}{lcl} \boldsymbol{\sigma} &=& \mathbf{C} : \boldsymbol{\varepsilon}_e \\ \pi^{\alpha}_r &=& 0 \\ \boldsymbol{\xi}^{\alpha} &=& X_0\, l^n_{en} \left[\left|\mathbf{s}^{\alpha} \cdot \boldsymbol{\kappa}^{\alpha}_r\right|^{n-2} \mathbf{s}^{\alpha} \otimes \mathbf{s}^{\alpha} + \left|\mathbf{l}^{\alpha} \cdot \boldsymbol{\kappa}^{\alpha}_r\right|^{n-2} \mathbf{l}^{\alpha} \otimes \mathbf{l}^{\alpha}\right] \cdot \boldsymbol{\kappa}^{\alpha}_r \end{array}\right. \tag{34}$$

It can be verified that $\boldsymbol{\xi}^{\alpha}$ is tangent to the slip plane α. In rate form, these laws can be written as (see Appendix A):

$$\left\{\begin{array}{lcl} \dot{\boldsymbol{\sigma}} &=& \mathbf{C} : \dot{\boldsymbol{\varepsilon}}_e \\ \dot{\pi}^{\alpha}_r &=& 0 \\ \dot{\boldsymbol{\xi}}^{\alpha} &=& \mathbf{A}^{\alpha\alpha} \cdot \dot{\boldsymbol{\kappa}}^{\alpha}_r \end{array}\right. \tag{35}$$

where $\mathbf{A}^{\alpha\alpha}$ is higher-order stiffness matrix associated with slip system α, defined by:

$$\mathbf{A}^{\alpha\alpha} = (n-1)\, X_0\, l_{en}^n \left[|\mathbf{s}^\alpha \cdot \boldsymbol{\kappa}_r^\alpha|^{n-2}\, \mathbf{s}^\alpha \otimes \mathbf{s}^\alpha + |\mathbf{l}^\alpha \cdot \boldsymbol{\kappa}_r^\alpha|^{n-2}\, \mathbf{l}^\alpha \otimes \mathbf{l}^\alpha \right] \tag{36}$$

2.4.2. Constitutive laws for the dissipative stresses

As suggested by (28), rate-dependent constitutive relations are used to describe the first-order dissipative stresses:

$$\pi_d^\alpha = S_\pi^\alpha \left[\frac{\dot{e}_\pi^\alpha}{\dot{\gamma}_0^\alpha} \right]^m \frac{\dot{\gamma}^\alpha}{\dot{e}_\pi^\alpha} \quad \text{with} \quad \dot{e}_\pi^\alpha = |\dot{\gamma}^\alpha| \tag{37}$$

where $\dot{\gamma}_0^\alpha > 0$ is a constant strain rate representative of the flow rates of interest, $m > 0$ is a constant characterizing the rate-sensitivity of the considered material, and S_π^α is the first-order dissipative slip resistance associated with slip system α. To model first-order hardening, the latter variable is assumed to evolve according to:

$$\dot{S}_\pi^\alpha = \sum_{\beta=1}^{q} h_\pi^{\alpha\beta} \left(S_\pi^\beta \right) \dot{e}_\pi^\beta \quad \text{with} \quad S_\pi^\alpha(0) = S_{\pi 0} > 0 \tag{38}$$

where $S_{\pi 0}$ is the initial first-order dissipative slip resistance assumed to be the same for all slip systems and $h_\pi^{\alpha\beta}$ is a first-order hardening function describing the interaction between slip systems α and β. In a similar manner, rate-dependent constitutive relations are used to describe the evolution of the equivalent higher-order stresses ($\xi_{eq}^\alpha = \|\boldsymbol{\xi}^\alpha\|$):

$$\xi_{eq}^\alpha = S_\xi^\alpha\, l_d \left(\frac{\dot{\kappa}_d^\alpha}{\dot{\gamma}_0^\alpha} \right)^m \quad \text{with} \quad \dot{\kappa}_d^\alpha = \|l_d\, \dot{\boldsymbol{\kappa}}_d^\alpha\| \tag{39}$$

where S_ξ^α is the higher-order dissipative slip resistance associated with slip system α. This variable is assumed to be governed by a higher-order hardening relation similar to that used for the first-order counterpart (S_π^α):

$$\dot{S}_\xi^\alpha = \sum_{\beta=1}^{q} h_\xi^{\alpha\beta} \left(S_\xi^\beta \right) \dot{\kappa}_{\mathrm{d}}^\beta \quad \text{with} \quad S_\xi^\alpha(0) = S_{\xi 0} \geq 0 \tag{40}$$

where $S_{\xi 0}$ is the initial higher-order dissipative slip resistance assumed to be the same for all slip systems and $h_\xi^{\alpha\beta}$ is a higher-order hardening function describing the interaction between slip systems α and β. Finally, the dissipative plastic slip gradient rates are assumed to obey normality-like flow rules as follows:

$$\dot{\boldsymbol{\kappa}}_d^\alpha = \frac{\dot{\kappa}_d^\alpha}{l_d} \frac{\boldsymbol{\xi}^\alpha}{\xi_{eq}^\alpha} \tag{41}$$

Due to the nonlinear dependence between $\boldsymbol{\xi}^\alpha$ and $\dot{\boldsymbol{\kappa}}_d^\alpha$, the higher-order microscopic stresses are determined at the integration points using local backward Euler scheme.

2.5. Reformulation of the microscopic equilibrium equations

When augmented by the constitutive laws of the microscopic stresses, the microscopic balance equation associated with slip system α $(7)_1$ becomes a flow rule for this system (Gurtin et al., 2007). Using Eq. $(34)_3$, it can be demonstrated that (see Appendix A):

$$\boldsymbol{\nabla} \cdot \boldsymbol{\xi}^\alpha \;=\; \mathbf{A}^{\alpha\alpha} : \boldsymbol{\nabla} \boldsymbol{\kappa}_r^\alpha \;= \mathbf{A}^{\alpha\alpha} : [\boldsymbol{\nabla} \boldsymbol{\kappa}^\alpha - \boldsymbol{\nabla} \boldsymbol{\kappa}_d^\alpha] \tag{42}$$

with $\mathbf{A}^{\alpha\alpha}$ given by (36). Substituting (37) and (42) into $(7)_1$, the flow rule for slip system α can be obtained:

$$\tau^{\alpha} \;-\; \underbrace{(-\mathbf{A}^{\alpha\alpha} : [\boldsymbol{\nabla}\boldsymbol{\kappa}^{\alpha} - \boldsymbol{\nabla}\boldsymbol{\kappa}_d^{\alpha}])}_{\text{(I) Backstress}} \;=\; \underbrace{S_{\pi}^{\alpha}\left[\frac{\dot{e}_{\pi}^{\alpha}}{\dot{\gamma}_0^{\alpha}}\right]^{m}\frac{\dot{\gamma}^{\alpha}}{\dot{e}_{\pi}^{\alpha}}}_{\text{(II) Dissipative hardening}} \tag{43}$$

Term (I), being recoverable, represents a backstress, leading to Bauschinger-like hardening effects. Term (II) represents first-order dissipative hardening effects (reversal of the flow direction $\dot{\gamma}^{\alpha} \rightarrow -\dot{\gamma}^{\alpha}$ simply changes the sign of this term). Contrary to classical Gurtin-type SG(C)P models (Gurtin et al., 2007), there is no explicit term representing higher-order dissipative hardening effects. These effects are implicitly considered with the help of the dissipative plastic slip gradients, which constrain the evolution of the backstresses.

3. Simplified two-dimensional version of the proposed SGCP model and numerical implementation

In this section, a simplified two-dimensional (2D) version of the proposed SGCP model is derived and implemented to study, in a simple manner, the influence of the involved higher-order dissipative parameters on the global response of materials.

3.1. Simplified 2D SGCP model

The 2D model is formulated assuming plane strain conditions in the plane $(\mathbf{e}_1, \mathbf{e}_2)$ and considering only planar slip systems verifying:

$$\mathbf{s}^{\alpha}\cdot\mathbf{e}_3 = 0, \quad \mathbf{m}^{\alpha}\cdot\mathbf{e}_3 = 0, \quad \mathbf{s}^{\alpha}\times\mathbf{m}^{\alpha} = -\mathbf{l}^{\alpha} = \mathbf{e}_3 \tag{44}$$

with the plastic slips γ^{α} independent of x_3. In this case, the plastic slip gradients $\boldsymbol{\nabla}\gamma^{\alpha}$ lie in the plane $(\mathbf{e}_1, \mathbf{e}_2)$ and the screw dislocations vanish:

$$\rho_{\odot}^{\alpha} = \mathbf{l}^{\alpha}\cdot\boldsymbol{\nabla}\gamma^{\alpha} = -\mathbf{e}_3\cdot\boldsymbol{\nabla}\gamma^{\alpha} = 0 \tag{45}$$

Prior to activation of the higher-order dissipation, it can be verified from Eq. $(34)_3$ that the higher-order microscopic stresses also lie in the plane $(\mathbf{e}_1, \mathbf{e}_2)$. Therefore, one can reasonably admit that the recoverable and unrecoverable parts of the plastic slip gradients develop in this plane:

$$\varrho_{\odot}^{\alpha} = \mathbf{l}^{\alpha}\cdot\boldsymbol{\kappa}_r^{\alpha} = 0, \quad \text{and} \quad \eta_{\odot}^{\alpha} = \mathbf{l}^{\alpha}\cdot\boldsymbol{\kappa}_d^{\alpha} = 0 \tag{46}$$

Ignoring the crystalline elastic anisotropy, the macroscopic and microscopic stresses involved in the simplified two-dimensional SGCP model can be expressed as:

$$\begin{aligned}
\boldsymbol{\sigma} &= \lambda\,\mathrm{tr}\,(\boldsymbol{\varepsilon}-\boldsymbol{\varepsilon}_p)\,\mathbf{I} + 2\,\mu\,(\boldsymbol{\varepsilon}-\boldsymbol{\varepsilon}_p)\\
\pi^{\alpha} &= S_{\pi}^{\alpha}\left[\frac{\dot{e}_{\pi}^{\alpha}}{\dot{\gamma}_0^{\alpha}}\right]^{m}\frac{\dot{\gamma}^{\alpha}}{\dot{e}_{\pi}^{\alpha}}\\
\boldsymbol{\xi}^{\alpha} &= X_0\,l_{en}^{n}\left[|\mathbf{s}^{\alpha}\cdot(\boldsymbol{\kappa}^{\alpha}-\boldsymbol{\kappa}_d^{\alpha})|^{n-2}\,\mathbf{s}^{\alpha}\otimes\mathbf{s}^{\alpha}\right]\cdot(\boldsymbol{\kappa}^{\alpha}-\boldsymbol{\kappa}_d^{\alpha})
\end{aligned} \tag{47}$$

with:

$$\begin{aligned}
\xi_{eq}^{\alpha} &= S_{\xi}^{\alpha}\,l_d\left(\frac{\dot{\kappa}_d^{\alpha}}{\dot{\gamma}_0^{\alpha}}\right)^{m}\\
\dot{\boldsymbol{\varepsilon}}_p &= \sum_{\alpha=1}^{q}\dot{\gamma}^{\alpha}\mathbf{P}^{\alpha}\\
\dot{\boldsymbol{\kappa}}_d^{\alpha} &= \frac{\dot{\kappa}_d^{\alpha}}{l_d}\frac{\boldsymbol{\xi}^{\alpha}}{\|\boldsymbol{\xi}^{\alpha}\|}
\end{aligned} \tag{48}$$

and λ and μ the Lamé elastic moduli. For simplicity, the first- and higher-order slip resistances S_π^α and S_ξ^α are assumed to evolve linearly with the first- and higher-order effective plastic slip measures:

$$\begin{aligned}
\dot{S}_\pi^\alpha &= \sum_{\beta=1}^{q} H_\pi \, \dot{e}_\pi^\beta \quad \text{with} \quad S_\pi^\alpha(0) = S_{\pi 0} > 0,\ H_\pi = \text{constant} \geq 0 \\
\dot{S}_\xi^\alpha &= \sum_{\beta=1}^{q} H_\xi \, \dot{\kappa}_d^\beta \quad \text{with} \quad S_\xi^\alpha(0) = S_{\xi 0} \geq 0,\ H_\xi = \text{constant} \geq 0
\end{aligned} \tag{49}$$

3.2. Numerical implementation

Let $\delta\dot{\mathbf{u}}$ and $\delta\dot{\boldsymbol{\gamma}}$ be virtual fields kinematically admissible to $\mathbf{0}$ on the portions of the studied domain boundary on which Dirichlet (essential) boundary conditions are applied. The weak forms of the macroscopic and microscopic balance equations, i.e., $(6)_1$ and $(7)_1$, can be written as:

$$\begin{aligned}
G_u &= \int_{\mathcal{V}} \delta\dot{\boldsymbol{\varepsilon}} : \boldsymbol{\sigma} \, dv - \int_{\mathcal{S}_t} \delta\dot{\mathbf{u}} \cdot \mathbf{t} \, ds \\
G_\gamma &= \sum_{\alpha=1}^{q} \int_{\mathcal{V}} \boldsymbol{\nabla}\delta\dot{\gamma}^\alpha \cdot \boldsymbol{\xi}^\alpha \, dv + \sum_{\alpha=1}^{q} \int_{\mathcal{V}} \delta\dot{\gamma}^\alpha \, \pi^\alpha \, dv - \sum_{\alpha=1}^{q} \int_{\mathcal{V}} \delta\dot{\gamma}^\alpha \, \tau^\alpha \, dv - \sum_{\alpha=1}^{q} \int_{\mathcal{S}_\chi^\alpha} \delta\dot{\gamma}^\alpha \, \chi^\alpha \, ds
\end{aligned} \tag{50}$$

where $\mathcal{S}_t$ and $\mathcal{S}_\chi^\alpha$ are respectively the portions of the studied domain boundary on which macroscopic and microscopic traction forces, respectively denoted by $\mathbf{t}$ and χ^α, are imposed. These weak forms are solved numerically using finite element method. To this end, a User-ELement (UEL) subroutine is implemented in ABAQUS/Standard, with the displacement and plastic slip fields ($\mathbf{u}$ and γ^α) considered as degrees of freedom. A finite element employing eight-noded $\mathbf{u}$-interpolation, four-noded γ^α-interpolation and 2×2 Gauss integration is considered. In this element, the displacement and plastic slip fields are approximated as:

$$u_i(x_1, x_2) = \sum_{k=1}^{8} N_k^u(x_1, x_2) \, U_i^k, \quad \gamma^\alpha(x_1, x_2) = \sum_{k=1}^{4} N_k^\gamma(x_1, x_2) \, \Gamma_k^\alpha \tag{51}$$

where U_i^k and Γ_k^α are respectively the nodal values of the displacement component u_i and the plastic slip γ^α, and N_k^u and N_k^γ are the associated interpolation (shape) functions. The aforementioned weak forms can then be approximated in matrix form within a representative finite element as follows:

$$\begin{aligned}
G_u^e &= \left(\delta\underline{\dot{U}}^e\right)^T \cdot \left(\int_{\mathcal{V}^e} \underline{\underline{B}}_u^T \cdot \underline{\sigma} \, dv - \int_{\mathcal{S}_t^e} \underline{\underline{N}}_u^T \cdot \underline{t} \, ds \right) \\
G_\gamma^e &= \left(\delta\underline{\dot{\Gamma}}^e\right)^T \cdot \left(\int_{\mathcal{V}^e} \underline{\underline{B}}_\gamma^T \cdot \underline{\xi} \, dv + \int_{\mathcal{V}^e} \underline{\underline{N}}_\gamma^T \cdot \underline{\pi} \, dv - \int_{\mathcal{V}^e} \underline{\underline{N}}_\gamma^T \cdot \underline{\tau} \, dv - \int_{\mathcal{S}_\chi^e} \underline{\underline{N}}_\gamma^T \cdot \underline{\chi} \, ds \right)
\end{aligned} \tag{52}$$

where $\underline{\sigma}$, $\underline{\pi}$ and $\underline{\xi}$ are vector representations of the macroscopic and microscopic stresses associated with all slip systems, $\underline{\tau}$ is a vector containing the resolved shear stresses on all slip systems, $\underline{t}$ is the macroscopic traction vector, $\underline{\chi}$ is a vector containing the microscopic traction scalars associated with all the slip systems, $\underline{\underline{N}}_u$ and $\underline{\underline{B}}_u$ are interpolation and gradient matrices associated with the displacement field, and $\underline{\underline{N}}_\gamma$ and $\underline{\underline{B}}_\gamma$ are interpolation and gradient matrices associated with the plastic slip fields. The principle of generalized virtual power implies that G_u^e and G_γ^e are zero for any virtual variations of the element nodal variables $\delta\underline{\dot{U}}^e$ and $\delta\underline{\dot{\Gamma}}^e$, which yields:

$$\begin{aligned}
\underline{R}_u^e &= \int_{\mathcal{V}^e} \underline{\underline{B}}_u^T \cdot \underline{\sigma} \, dv - \int_{\mathcal{S}_t^e} \underline{\underline{N}}_u^T \cdot \underline{t} \, ds = \underline{0} \\
\underline{R}_\gamma^e &= \int_{\mathcal{V}^e} \underline{\underline{B}}_\gamma^T \cdot \underline{\xi} \, dv + \int_{\mathcal{V}^e} \underline{\underline{N}}_\gamma^T \cdot \underline{\pi} \, dv - \int_{\mathcal{V}^e} \underline{\underline{N}}_\gamma^T \cdot \underline{\tau} \, dv - \int_{\mathcal{S}_\chi^e} \underline{\underline{N}}_\gamma^T \cdot \underline{\chi} \, ds = \underline{0}
\end{aligned} \tag{53}$$

These equations are linearized with respect to the variations of the element nodal variables $\underline{U}^e$ and $\underline{\Gamma}^e$, which results in an elementary system of equations that can be presented in matrix form as:

$$\begin{bmatrix} \underline{\underline{K}}^e_{uu} & \underline{\underline{K}}^e_{u\gamma} \\ \underline{\underline{K}}^e_{\gamma u} & \underline{\underline{K}}^e_{\gamma\gamma} \end{bmatrix} \begin{bmatrix} \Delta\underline{U}^e \\ \Delta\underline{\Gamma}^e \end{bmatrix} = \begin{bmatrix} -\underline{R}^e_u \\ -\underline{R}^e_\gamma \end{bmatrix} \tag{54}$$

with:

$$\underline{\underline{K}}^e_{uu} = \frac{\partial \underline{R}^e_u}{\partial \underline{U}^e}, \quad \underline{\underline{K}}^e_{u\gamma} = \frac{\partial \underline{R}^e_u}{\partial \underline{\Gamma}^e}, \quad \underline{\underline{K}}^e_{\gamma u} = \frac{\partial \underline{R}^e_\gamma}{\partial \underline{U}^e}, \quad \underline{\underline{K}}^e_{\gamma\gamma} = \frac{\partial \underline{R}^e_\gamma}{\partial \underline{\Gamma}^e} \tag{55}$$

The overall elementary systems are assembled to obtain the global system of equations which is solved using Newton-Raphson iterative scheme. At each iteration, updated values of displacement and plastic slip increments ($\Delta\underline{U}$ and $\Delta\underline{\Gamma}$, respectively) are obtained and used to solve numerically the constitutive equations at the Gauss points (Alg. 1).

4. Parametric study and numerical results

To investigate the influence of the major constitutive parameters involved in the proposed SGCP model, the simplified 2D version of this model is applied to simulate simple shear tests. A 2D crystalline strip having infinite width in $\mathbf{e}_1$ direction and height h in $\mathbf{e}_2$ direction is considered, with two active slip systems symmetrically oriented with respect to $\mathbf{e}_1$ direction ($\theta_1 = -\theta_2 = 60°$), as illustrated in Fig. 1. The associated numerical sample consists of 1×100 finite elements (quadratic displacements and linear plastic slips) with periodic boundary conditions imposed on its left ($x_1 = 0$) and right ($x_1 = w$) edges:

$$\begin{array}{l} u_i\left(0, x_2, t\right) = u_i\left(w, x_2, t\right), \quad \text{for } i = 1,\ 2 \quad \forall\, x_2 \\ \gamma^\alpha\left(0, x_2, t\right) = \gamma^\alpha\left(w, x_2, t\right), \quad \text{for } \alpha = 1,\ 2 \quad \forall\, x_2 \end{array} \tag{56}$$

The bottom edge ($x_2 = 0$) is macro-clamped and the top edge ($x_2 = h$) is submitted to a cycle of loading-unloading displacement in $\mathbf{e}_1$ direction:

$$u_1(x_1, 0, t) = u_2(x_1, 0, t) = 0,\ u_1(x_1, h, t) = h\Gamma\left(t\right),\ \text{and}\ u_2(x_1, h, t) = 0 \quad \forall\, x_1 \tag{57}$$

where Γ is the prescribed shear strain ($0 \rightarrow 0.01 \rightarrow -0.01 \rightarrow 0.01$). In order to establish proportional and non-proportional loading conditions, which are necessary to better investigate certain gradient effects, three cases of microscopic (slip) boundary conditions are also considered on the top and bottom edges: proportional loading, one-side non-proportional loading and two-side non-proportional loading. In the first case, both edges are passivated over the entire simulation:

$$\gamma^\alpha(x_1, 0, t) = \gamma^\alpha(x_1, h, t) = 0, \quad \text{for } \alpha = 1,\ 2 \quad \forall\, x_1 \tag{58}$$

In the case of one-side non-proportional loading, the bottom edge is passivated over the entire simulation and the top edge is kept micro-free until prescribed shear strain $\Gamma = 0.005$ and then passivated until the end of the simulation:

$$\gamma^\alpha(x_1, 0, t) = 0,\ \dot{\gamma}^\alpha\left(x_1, h, t > t_0\right) = 0, \quad \text{for } \alpha = 1,\ 2 \quad \forall\, x_1 \tag{59}$$

where t_0 is the passivation time, *i.e.,* time at which $\Gamma\left(t_0\right) = 0.005$. Finally, in the case of two-side non-proportional loading, both edges are kept micro-free until prescribed shear strain $\Gamma = 0.005$ and then passivated until the end of the simulation:

Algorithm 1 Integration of the constitutive equations at the integration points

Inputs: $\boldsymbol{\varepsilon}_e$, $\boldsymbol{\varepsilon}_p$, $\boldsymbol{\kappa}_r^\alpha$, $\boldsymbol{\kappa}_d^\alpha$, $\Delta\mathbf{u}$, $\Delta\gamma^\alpha$, S_π^α, S_ξ^α, $\boldsymbol{\sigma}$, π^α, $\boldsymbol{\xi}^\alpha$

Compute: $\Delta\boldsymbol{\varepsilon} = [\nabla(\Delta\mathbf{u})]_{sym}$, $\Delta\boldsymbol{\varepsilon}_p = \sum_{\alpha=1}^{q} \Delta\gamma^\alpha \mathbf{P}^\alpha$, $\Delta\boldsymbol{\varepsilon}_e = \Delta\boldsymbol{\varepsilon} - \Delta\boldsymbol{\varepsilon}_p$

Compute: $\boldsymbol{\varepsilon}_e = \boldsymbol{\varepsilon}_e + \Delta\boldsymbol{\varepsilon}_e$, $\boldsymbol{\varepsilon}_p = \boldsymbol{\varepsilon}_p + \Delta\boldsymbol{\varepsilon}_p$

Compute: $\boldsymbol{\sigma} = \lambda \operatorname{tr}(\boldsymbol{\varepsilon}_e)\, \mathbf{I} + 2\,\mu\,\boldsymbol{\varepsilon}_e$

Do $\alpha = 1$ **to** q**:**

Compute: $\Delta e_\pi^\alpha = |\Delta\gamma^\alpha|$

End do

Do $\alpha = 1$ **to** q**:**

Compute: $\Delta S_\pi^\alpha = \sum_{\beta}^{q} H_\pi\, \Delta e_\pi^\beta$

Compute: $S_\pi^\alpha = S_\pi^\alpha + \Delta S_\pi^\alpha$

Compute: $\pi^\alpha = S_\pi^\alpha \left[\frac{\Delta e_\pi^\alpha}{\Delta t\, \dot{\gamma}_0^\alpha}\right]^m \frac{\Delta\gamma^\alpha}{\Delta e_\pi^\alpha}$

End do

Initialization:

Do $\alpha = 1$ **to** q**:**

Compute: $\Delta\boldsymbol{\kappa}^\alpha = \nabla(\Delta\boldsymbol{\gamma}^\alpha)$, $\Delta\boldsymbol{\kappa}_r^\alpha = \Delta\boldsymbol{\kappa}^\alpha$, $\boldsymbol{\kappa}_r^\alpha = \boldsymbol{\kappa}^\alpha + \Delta\boldsymbol{\kappa}_r^\alpha$, $\Delta\boldsymbol{\kappa}_d^\alpha = \mathbf{0}$, $\Delta\kappa_d^\alpha = 0$

Compute: $\mathbf{A}^{\alpha\alpha} = (n-1)\; X_0\, l_{en}^n\; |\boldsymbol{s}^\alpha \cdot \boldsymbol{\kappa}_r^\alpha|^{n-2}\; \boldsymbol{s}^\alpha \otimes \boldsymbol{s}^\alpha$

Compute: $\Delta\boldsymbol{\xi}^\alpha = \mathbf{A}^{\alpha\alpha} \cdot \Delta\boldsymbol{\kappa}_r^\alpha$, $\boldsymbol{\xi}^\alpha = \boldsymbol{\xi}^\alpha + \Delta\boldsymbol{\xi}^\alpha$

Compute: $F^\alpha = \|\boldsymbol{\xi}^\alpha\|$

End do

$\mathbf{F} = \left[F^1, ..., F^q\right]^T$

End initialization

While ($\|\mathbf{F}\| > \varepsilon$)**:**

Solve:
$$\begin{bmatrix} \frac{\partial F^1}{\partial \kappa_d^1} & \cdot & \cdot & \cdot & \frac{\partial F^1}{\partial \kappa_d^q} \\ \cdot & \cdot & & & \cdot \\ \cdot & & \cdot & & \cdot \\ \cdot & & & \cdot & \cdot \\ \frac{\partial F^q}{\partial \kappa_d^1} & \cdot & \cdot & \cdot & \frac{\partial F^q}{\partial \kappa_d^q} \end{bmatrix} \cdot \begin{Bmatrix} \delta\kappa_d^1 \\ \cdot \\ \cdot \\ \cdot \\ \delta\kappa_d^q \end{Bmatrix} = \begin{Bmatrix} F^1 \\ \cdot \\ \cdot \\ \cdot \\ F^q \end{Bmatrix}$$

Do $\alpha = 1$ **to** q**:**

Update: $\Delta\kappa_d^\alpha$, $\Delta\boldsymbol{\kappa}_d^\alpha$, $\boldsymbol{\kappa}_d^\alpha$, $\Delta\boldsymbol{\kappa}_r^\alpha$, $\boldsymbol{\kappa}_r^\alpha$

Update: $\boldsymbol{\xi}^\alpha$, S_ξ^α

Update: $F^\alpha = \|\boldsymbol{\xi}^\alpha\| - S_\xi^\alpha\, l_d \left(\frac{\Delta\kappa_d^\alpha}{\Delta t\, \dot{\gamma}_0^\alpha}\right)^m$

End do

$\mathbf{F} = \left[F^1, ..., F^q\right]^T$

End while

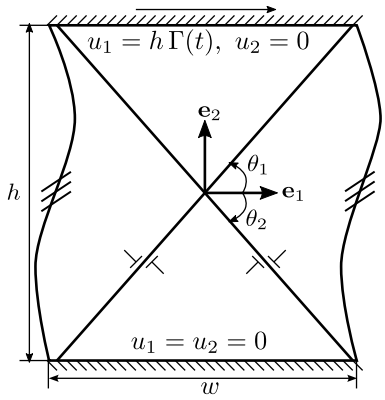

Fig. 1. Geometrical model for simple shear simulations: 2D crystalline strip with two active slip systems symmetrically oriented with respect to $\mathbf{e}_1$ ($\theta_1 = -\theta_2 = 60°$).

Tab. 1. Material parameters used in this work, inspired by Gurtin et al. (2007).

Material parameter name	Symbol	Value	Unit
First Lamé elastic modulus	λ	150	GPa
Second Lamé elastic modulus	μ	100	GPa
Reference slip rate	$\dot{\gamma}_0^\alpha$	0.04	s^{-1}
Rate-sensitivity parameter	m	0.01	–
Higher-order energetic slip resistance	X_0	50	MPa
Initial first-order dissipative slip resistance	$S_{\pi 0}$	50	MPa
First-order hardening modulus	H_π	0	MPa
Defect energy index	n	case study	–
Energetic length scale	l_{en}	case study	μm
Dissipative length scale	l_d	case study	μm
Initial higher-order dissipative slip resistance	$S_{\xi 0}$	case study	MPa
Higher-order hardening modulus	H_ξ	case study	MPa

$$\dot{\gamma}^\alpha(x_1, 0, t > t_0) = \dot{\gamma}^\alpha\,(x_1, h, t > t_0) = 0, \quad \text{for } \alpha = 1,\, 2 \qquad \forall\, x_1 \tag{60}$$

Contrary to the last non-proportional loading case, in the case of one-side non-proportional loading, nonuniform plastic strain distribution develops within the strip before activation of the non-proportional loading source (top edge passivation). This allows for a more complete investigation of the higher-order effects under non-proportional loading conditions. The material parameters used in this work are given in Tab. 1, in which the fixed values are inspired by Gurtin et al. (2007).

4.1. Case of quadratic defect energy

The classical case of quadratic defect energy ($n = 2$) is first considered to investigate, in a simple manner, the influence of the higher-order dissipative parameters involved in the proposed model. In this case, the energetic length scale l_{en} only influences the kinematic hardening rate after yielding (Gurtin et al., 2007; Jebahi et al., 2020). Therefore, this parameter must be carefully chosen to ensure clear activation of the higher-order dissipative effects in the considered loading range. Indeed, using small rate-sensitivity parameter $m = 0.01$, such effects are significantly activated only when the higher-order stresses verify $\xi_{eq}^\alpha \geq S_{\xi 0}\, l_d$.

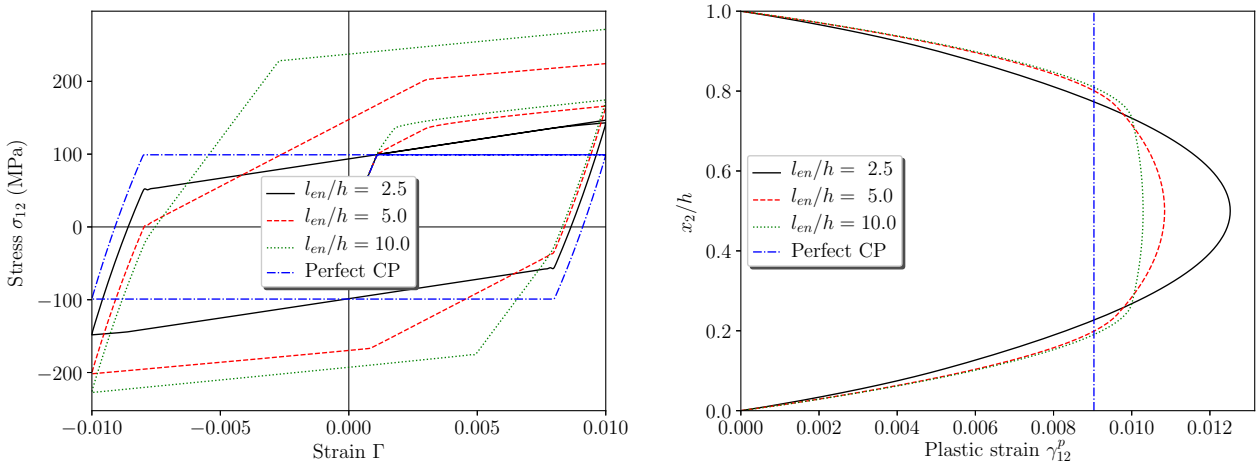

(a) Stress-Strain curves.

(b) Plastic shear strain profile along $\mathbf{e}_2$ direction.

Fig. 2. Simple shear response for different values of the energetic length scale l_{en} in the presence of higher-order dissipation ($n = 2$, $l_d/h = 1$, $S_{\xi 0} = 10\,\text{MPa}$, $H_\xi = 100\,\text{MPa}$).

Fig. 2 presents the shear response results in terms of stress-strain curves and plastic shear strain distributions along the strip thickness for different values of l_{en}, with dissipative length scale $l_d = h$ and initial higher-order dissipative slip resistance $S_{\xi 0} = 10\,\text{MPa}$. Results obtained using classical crystal plasticity (CP) are also presented in this figure, for comparison purposes. Using small l_{en} (case of $l_{en} = 2.5\,h$), almost non-dissipative higher-order response is obtained, with only kinematic hardening effects and quadratic distribution of plastic shear strain along the thickness of the studied strip. However, using large l_{en} (case of $l_{en} \geq 5\,h$), two plastic regimes can be distinguished after the initial yielding. Relatively steep-sloped plastic evolution appears immediately beyond the classical crystal plasticity (CP) yield stress, which is referred to hereafter as first-order yield stress. Then, an abrupt decrease in the plastic slope is observed at a further yield stress, corresponding to activation of the higher-order dissipative effects. This yield stress is referred to hereafter as higher-order yield stress. It should be noted that the obtained two-stage plastic behavior is rather unusual. This idealized behavior is due to the simplicity of the considered two-dimensional shear sample with only two symmetric planar slip systems, as well as to the considered set of model parameters with quadratic defect energy density. Activation of the higher-order dissipation leads to dissipative (isotropic-like) hardening effects (Fig. 2a). As shown in Fig. 2b, this results in a flattening of the plastic shear strain distribution and in a reduction of the thickness of the boundary layers, *i.e.,* small regions near the passivated edges characterized by rapid spatial evolution of the plastic shear strain.

Unless otherwise specified, the energetic length scale l_{en} is set equal to $l_{en} = 10\,h$ in the remainder of the present subsection. This leads to a rapid increase of the higher-order stresses after the first-order yielding, making it possible to activate the higher-order dissipation in the considered loading range.

4.1.1. Influence of the higher-order dissipative parameters

Effects of the higher-order dissipative parameters, namely the dissipative length scale l_d, the initial higher-order slip resistance $S_{\xi 0}$ and the higher-order hardening parameter H_ξ, are investigated hereafter using proportional shear loading conditions.

Fig. 3 shows the influence of the dissipative length scale l_d on the shear response of the considered strip, for constant $S_{\xi 0} = 10\,\text{MPa}$ and $H_\xi = 100\,\text{MPa}$. It can be observed from the stress-strain curves (Fig. 3a) that l_d affects both the higher-order yield stress, at which the higher-order dissipation is activated, and the hardening rate after the higher-order yielding. The larger this parameter, the larger are the higher-order yield

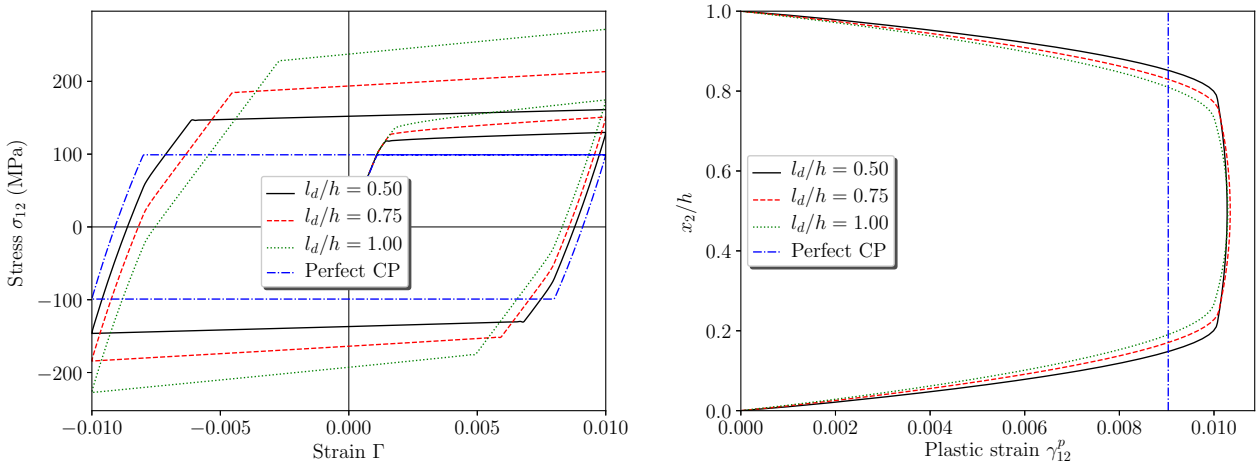

(a) Stress-Strain curves.

(b) Plastic shear strain profile along $\mathbf{e}_2$ direction.

Fig. 3. Simple shear response for different values of the dissipative length scale l_d ($n = 2$, $l_{en}/h = 10$, $S_{\xi 0} = 10\,\mathrm{MPa}$, $H_\xi = 100\,\mathrm{MPa}$).

stress and hardening slope. Analysis of the stress-strain curves under reverse loading shows the dissipative (isotropic-like) nature of the obtained hardening behavior beyond the higher-order yielding. In terms of plastic shear strain evolution along the strip thickness (Fig. 3b), applying non-zero $S_{\xi 0}$, the dissipative length scale l_d leads to relatively non-smooth profiles, with narrow boundary layers in the vicinity of the passivated edges and nearly plateau-shaped plastic distribution beyond the layers. As shown in Fig. 3b, increasing l_d results in larger boundary layers. However, outside these layers, the plastic shear strain distributions, as well as the associated maximum values, seem nearly insensitive to this parameter. It should be noted that the obtained profiles in Fig. 3b are in accordance with those obtained using the Gurtin-type model of Jebahi et al. (2020) within comparable higher-order conditions. The latter model is based on the classical additive decomposition of the higher-order stresses into recoverable and dissipative parts. The proposed plastic slip gradient decomposition does not seem to influence the manner in which the plastic shear strains are distributed along the strip thickness.

Fig. 4 presents the effects of the initial higher-order slip resistance $S_{\xi 0}$, for constant dissipative length scale $l_d = 0.5\,h$ and higher-order hardening parameter $H_\xi = 100\,\mathrm{MPa}$. It can be observed from the stress-strain results (Fig. 4a) that $S_{\xi 0}$ only influences the higher-order yield stress, with no effects on the hardening slope after the higher-order yielding. Decreasing $S_{\xi 0}$ makes the higher-order yield stress tend towards the first-order one, *i.e.,* the classical CP yield stress. Using $S_{\xi 0} = 0.01\,\mathrm{MPa}$ (a small value is actually needed instead of zero to avoid numerical convergence difficulties), the higher-order dissipation is nearly activated from the beginning of plasticity (Fig. 4a). In terms of plastic shear strain profiles (Fig. 4b), $S_{\xi 0}$ influences both the width of the boundary layers and the plastic shear strain plateau value, which increase with decreasing $S_{\xi 0}$. By using smaller $S_{\xi 0}$, the dissipative higher-order effects are activated at smaller higher-order yield stress, leading to lower resistance to plastic flow and then larger plastic shear strain levels with more regular profile. The case of $S_{\xi 0} = 0.01\,\mathrm{MPa}$ yields nearly quadratic plastic shear strain distribution, whose form is quite similar to that obtained assuming purely recoverable effects (Gurtin et al., 2007; Jebahi et al., 2020). In this case, the recoverable and dissipative higher-order effects are activated at the same (first-order) yield stress, leading to smooth evolution of the microscopic higher-order stresses as when considering only recoverable effects.

Fig. 5 provides a further comparison between the effects of $S_{\xi 0}$ and l_d, for constant higher-order hardening parameter $H_\xi = 100\,\mathrm{MPa}$. Using two combinations of these parameters presenting the same $S_{\xi 0}\,l_d$

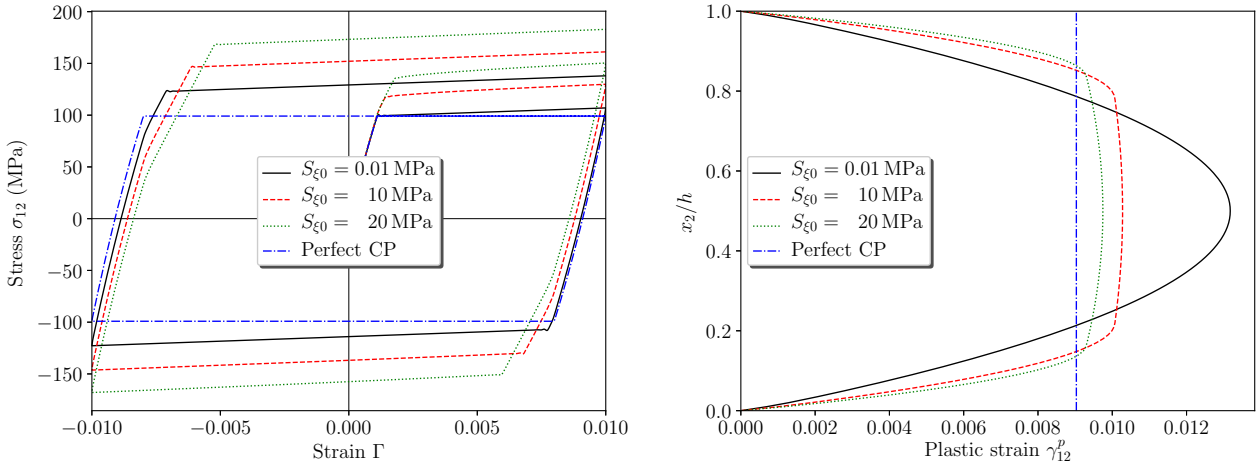

(a) Stress-Strain curves.

(b) Plastic shear strain profile along $\mathbf{e}_2$ direction.

Fig. 4. Simple shear response for different values of the initial higher-order slip resistance $S_{\xi 0}$ ($n = 2$, $l_{en}/h = 10$, $l_d/h = 0.5$, $H_\xi = 100\,\mathrm{MPa}$).

product (*e.g.,* $\{S_{\xi 0} = 10\,\mathrm{MPa},\ l_d = 0.5\,h\}$ and $\{S_{\xi 0} = 5\,\mathrm{MPa},\ l_d = h\}$), the higher-order dissipative effects are activated at the same higher-order yield point (Fig. 5a). However, beyond this point, different hardening slopes are obtained, which explain the differences in the associated plastic shear strain distributions (Fig. 5b). Regardless of the value of $S_{\xi 0}$, the combination with larger l_d yields larger hardening rate after the higher-order yielding. As for the plastic shear strain profiles, independently of the value of l_d, the combination with lower $S_{\xi 0}$ results in larger boundary layers and plastic shear strain plateau value.

Another important parameter conditioning the higher-order dissipation is the higher-order hardening parameter H_ξ $(49)_2$, which is taken as constant in the previous paragraphs ($H_\xi = 100\,\mathrm{MPa}$). Effects of this parameter are presented in Fig. 6, which is obtained using constant $l_d = 0.5\,h$ and $S_{\xi 0} = 10\,\mathrm{MPa}$. Considering the stress-strain results (Fig. 6a), H_ξ increases the plastic slope beyond the higher-order yielding. As shown under reverse loading, this parameter yields dissipative (isotropic-like) hardening behavior. In terms of plastic shear strain distributions (Fig. 6b), H_ξ influences both the width of the boundary layers and the plastic shear strain plateau value beyond these layers. The smaller the value of H_ξ, the smaller are these width and plateau value. Applying no higher-order hardening ($H_\xi = 0$), the higher-order stresses stop evolving beyond the higher-order yield point (*i.e.,* when $\xi^\alpha_{eq} = S_{\xi 0}\, l_d$). The associated plastic shear strain distribution (black curve in Fig. 6b), with very narrow boundary layers (their width corresponds to that of a finite element) and nearly constant plastic shear strain outside them, is close to that obtained using perfect crystal plasticity. The small differences are caused by the higher-order recoverable effects, which are not constant over the strip thickness due to the passivation conditions applied on the top and bottom edges.

4.1.2. Size effects in the presence of higher-order dissipation

Effects of the strip height h on the simple shear results are investigated hereafter, for constant higher-order dissipative parameters ($l_d = 0.5\,h$, $S_{\xi 0} = 10\,\mathrm{MPa}$ and $H_\xi = 100\,\mathrm{MPa}$). The investigation results are given in Fig. 7a, with zooming-in on the yielding region.

Contrary to classical Gurtin-type SG(C)P models including higher-order dissipation (Gurtin et al., 2007; Jebahi et al., 2020), the present model predicts no true elastic gaps at the initial yield. The apparent strengthening as a function of h, observed at this yield, is due to two-stage plastic behavior resulting from the competition between the recoverable and dissipative higher-order effects. As shown in the zoomed-in view of Fig. 7a, the first plastic stage always starts at the same initial yield point, which corresponds to the classical CP

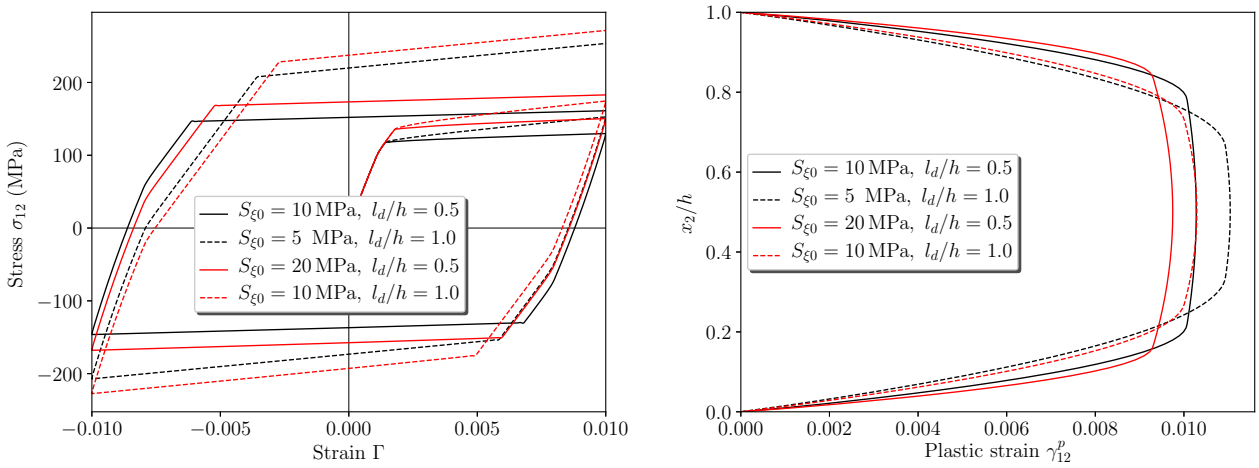

(a) Stress-Strain curves. **(b)** Plastic shear strain profile along $\mathbf{e}_2$ direction.

Fig. 5. Comparison between the effects of the initial higher-order slip resistance $S_{\xi 0}$ and the dissipative length scale l_d ($n = 2$, $l_{en}/h = 10$, $H_\xi = 100\,\text{MPa}$).

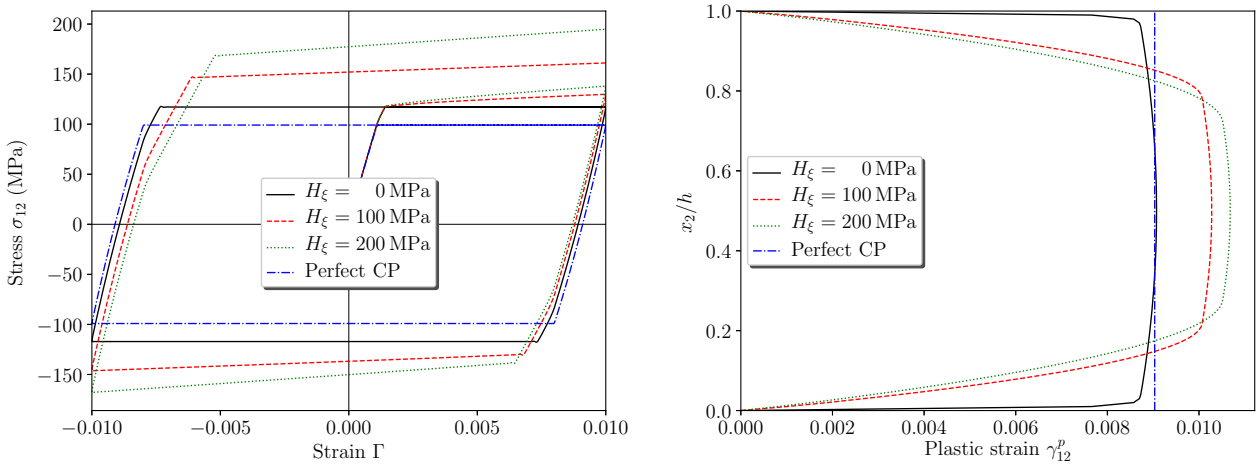

(a) Stress-Strain curves. **(b)** Plastic shear strain profile along $\mathbf{e}_2$ direction.

Fig. 6. Simple shear response for different values of the higher-order hardening parameter H_ξ ($n = 2$, $l_{en}/h = 10$, $l_d/h = 0.5$, $S_{\xi 0} = 10\,\text{MPa}$).

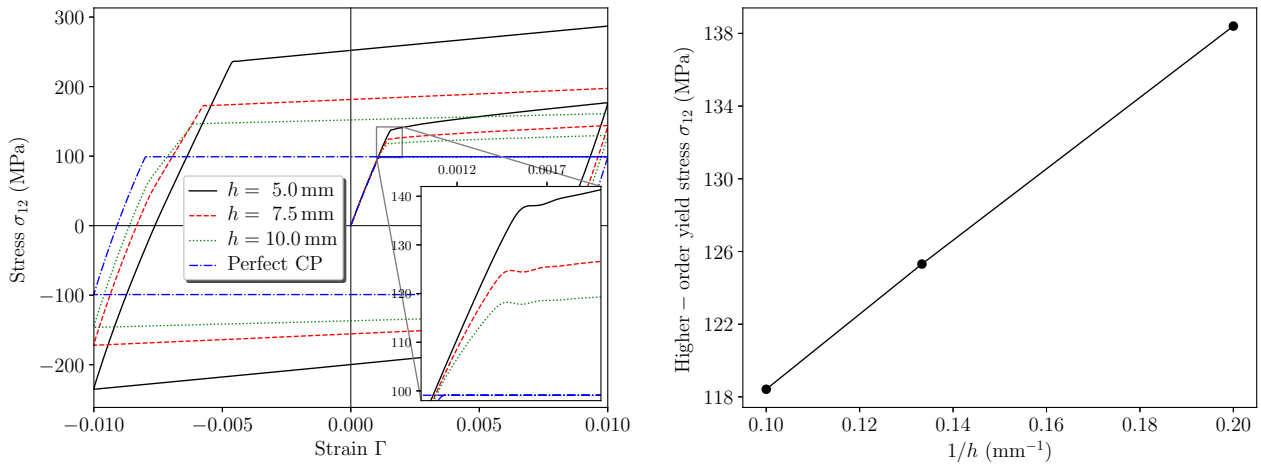

(a) Stress-Strain curves.

(b) Evolution of the higher-order yield stress with h.

Fig. 7. Influence of the strip height h on the strip simple shear response ($n = 2$, $l_{en} = 100\,\text{mm}$, $l_d = 5\,\text{mm}$, $S_{\xi 0} = 10\,\text{MPa}$, $H_\xi = 100\,\text{MPa}$).

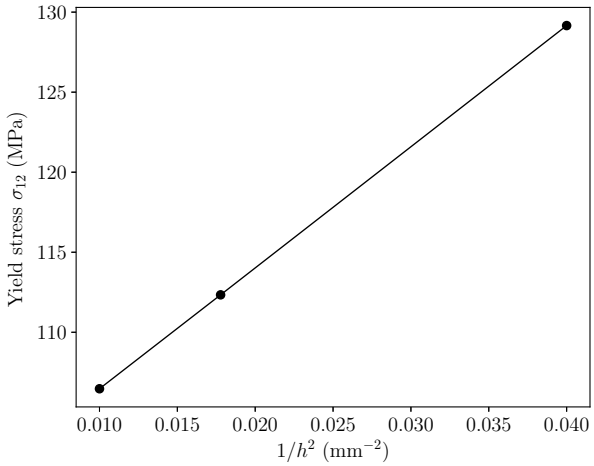

Fig. 8. Evolution of the yield stress measured at 0.2% plastic deformation with h: case of no higher-order dissipation ($n = 2$, $l_{en} = 20\,\text{mm}$, $l_d = 0$).

yield point, regardless of the strip thickness. The latter parameter only influences the plastic slope after the initial yielding, during the first plastic stage. Using smaller h, larger plastic slip gradients develop along the strip thickness, leading to larger higher-order recoverable stresses and steeper plastic evolution. Concerning the second plastic stage, the geometrical parameter h remarkably influences both the higher-order yield stress (activation of the higher-order dissipation) and the hardening rate beyond the higher-order yielding. According to Fig. 7b, the higher-order yield stress increases linearly with the reciprocal of h ($\propto h^{-1}$). The obtained -1 exponent scaling law is in accordance with the well-known Orowan relation for precipitate size effects. This law also complies with recent experimental investigations of size effects which show that the size dependence exponent could vary between -1 and -0.5 (De Sansal et al., 2010; Cordero et al., 2016; Jiang et al., 2019), or also between -1 and -0.2 (Dunstan and Bushby, 2014). It should be noted that, in the absence of higher-order dissipation (in such a case the proposed model reduces to a classical Gurtin-type SGCP model with only recoverable higher-order effects), the yield stress measured at 0.2% plastic deformation presents -2 exponent dependence with h ($\propto h^{-2}$), as shown in Fig. 8 and discussed in Forest and Guéninchault (2013).

Results of Fig. 7 show that, using an appropriate choice of the energetic and dissipative length scales, the proposed model is capable of capturing strengthening-like effects at the beginning of plasticity. Unlike in classical Gurtin-type SGP theories, these effects are not caused by the occurrence of true elastic gaps at the initial yield, but by the competition between high-level recoverable effects and softening capabilities of the dissipative ones.

4.2. Case of non-quadratic defect energy

Results of subsection 4.1 are obtained assuming quadratic defect energy. Although widely used in the literature (Gurtin, 2002, 2004; Gurtin et al., 2007; Panteghini and Bardella, 2016, 2018; Jebahi and Forest, 2021), the pertinence of this form of defect energy in the context of gradient-enhanced plasticity is questioned by several authors (Svendsen and Bargmann, 2010; Cordero et al., 2010; Forest and Guéninchault, 2013; Wulfinghoff et al., 2015). The present subsection aims at investigating the effects of the proposed plastic slip gradient decomposition using less-than-quadratic defect energy (*i.e.,* less-than-two defect energy index n).

For comparison purposes, the case with no higher-order dissipation is first analyzed (case of $l_d = 0$ in Fig. 9). Using less-than-quadratic defect energy, the simple shear response of the studied strip is characterized by a rapid increase followed by a rapid decrease in the evolution of the macroscopic shear stress at the initial yield. This is due to a similar evolution of the higher-order recoverable stresses $\boldsymbol{\xi}^{\alpha}$ in the vicinity of their singularity at zero plastic slip gradients. The obtained effect at the initial yield is often qualified as a strengthening in the literature (Panteghini and Bardella, 2018; Forest et al., 2019; El-Naaman et al., 2019). Analysis of the stress-strain response under a complete loading-unloading cycle shows that less-than-two defect energy index n leads to nonlinear kinematic hardening with inflection points, at which the plastic slip gradients cross zero (Wulfinghoff et al., 2015; El-Naaman et al., 2019; Jebahi et al., 2020). The obtained hardening is known as KIII kinematic hardening of Asaro (1975). Effects of the higher-order dissipation on this hardening behavior is investigated hereafter. Due to the rapid increase of the higher-order stresses at beginning of plasticity, there is no need for a large l_{en} to amplify the high-order recoverable effects. This parameter is then set equal to $l_{en} = 1$ in the remainder of this subsection.

Fig. 9 presents the effects of the dissipative length scale l_d in the case of less-than-quadratic defect energy ($n = 1.5$), assuming constant $S_{\xi 0} = 10\,\mathrm{MPa}$ and $H_{\xi} = 100\,\mathrm{MPa}$. In this figure, the stress-strain result obtained using $l_d = 0$ (*i.e.,* with no higher-order dissipation) also corresponds to sufficiently large l_d, for which the higher-order dissipation is not activated in the considered loading range. By decreasing l_d, earlier activation of the higher-order dissipation is obtained, after which the plastic behavior is controlled by the higher-order dissipative effects. This results in a narrower inflection region under reverse loading, which

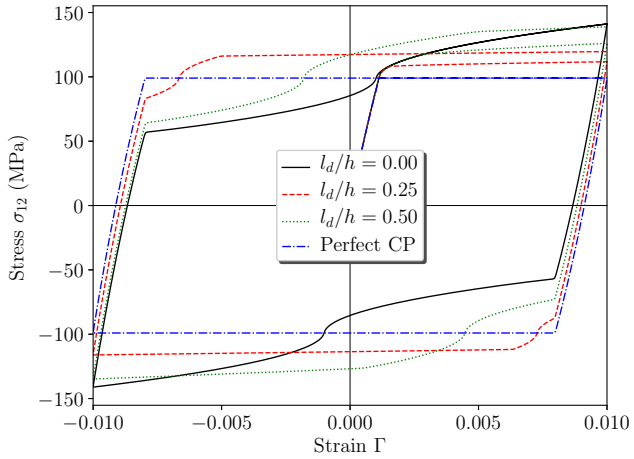

Fig. 9. Effects of the dissipative length scale l_d in the case of non-quadratic defect energy ($n = 1.5$, $l_{en}/h = 1$, $S_{\xi 0} = 10\,\mathrm{MPa}$, $H_\xi = 100\,\mathrm{MPa}$).

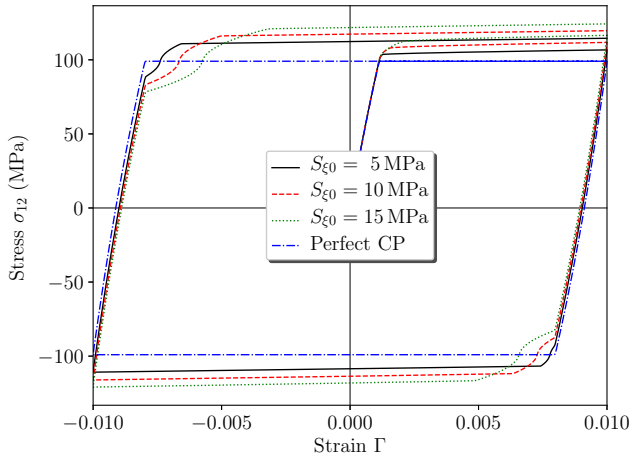

Fig. 10. Effects of the initial higher-order slip resistance $S_{\xi 0}$ in the case of non-quadratic defect energy ($n = 1.5$, $l_{en}/h = 1$, $l_d/h = 0.25$, $H_\xi = 100\,\mathrm{MPa}$).

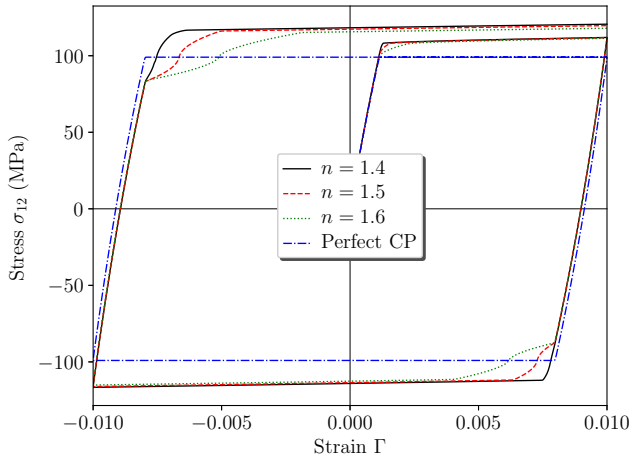

Fig. 11. Effects of the defect energy index n for constant higher-order dissipative parameters ($l_{en}/h = 1$, $l_d/h = 0.25$, $S_{\xi 0} = 10\,\mathrm{MPa}$, $H_\xi = 100\,\mathrm{MPa}$).

mirrors the region of the nonlinear increase of the higher-order stresses before activation of the higher-order dissipation. After the higher-order yielding, classical dissipative (isotropic-like) hardening behavior is obtained, for which the hardening slope decreases with decreasing l_d. As shown in Fig. 10, the width of the inflection region under reverse loading can also be reduced by decreasing the initial higher-order dissipative slip resistance $S_{\xi 0}$, which presents similar effects as l_d on the activation of the higher-order dissipation. However, similarly to when decreasing l_d, this produces lower global dissipative hardening levels.

Fig. 11 shows the stress-stain shear results for different less-than-two n and constant higher-order dissipative parameters ($l_d = 0.25\,h$, $S_{\xi 0} = 10\,\mathrm{MPa}$, $H_\xi = 100\,\mathrm{MPa}$). Smaller n induces a more rapid nonlinear increase of the higher-order stresses at the beginning of the plasticity. Therefore, smaller evolution zone is needed to reach the higher-order yield stress, and then to activate the higher-order dissipation. For sufficiently small n (*i.e.,* close to 1), the inflection region becomes nearly invisible, with no unusual effects on the hardening rate beyond the apparent (higher-order) yield stress. This provides another way for the proposed SGCP model to reproduce strengthening-like effects at the beginning of plasticity, while obtaining nearly classical response at the macroscopic scale (*i.e.,* with no apparent inflection regions).

4.3. Comparison with the Gurtin-type model of Jebahi et al. (2020)

The present subsection aims at comparing the proposed plastic slip gradient decomposition with the higher-order stress decomposition used in classical Gurtin-type gradient theories. To this end, results obtained using the present SGCP model are compared with those obtained using the Gurtin-type SGCP model presented in Jebahi et al. (2020), considering the proportional and non-proportional shear loading conditions detailed at the beginning of section 4. Quadratic defect energy ($n = 2$) is used in this present comparison study which mainly focuses on the formation of elastic gaps (delays in the plastic flow). Furthermore, the energetic length scale is set equal to $l_{en} = 5\,h$. This choice makes it possible to generate sufficient higher-order recoverable effects, while allowing for an easy distinction between a true elastic gap and a steep-sloped plastic evolution in the absence of higher-order dissipation.

Starting with the case of proportional loading conditions, Fig. 12 presents the comparison results obtained with and without higher-order dissipation. Ignoring the higher-order dissipative effects (Fig. 12a), the two models predict exactly the same results. Although not implemented in the same manner, the models are identical from a theoretical point of view in the case of zero l_d. However, quite different results are obtained when activating the higher-order dissipation (Fig. 12b). The Gurtin-type model predicts an elastic gap at the initial yield before the beginning of plasticity. Both recoverable and dissipative higher-order effects contribute to the relatively steep-sloped hardening behavior after yielding, as pointed out in Jebahi et al. (2020). On the contrary, using the present model, two-stage plastic behavior starts at the initial yield, with no elastic gap. During the first plastic stage, only higher-order recoverable effects are involved. The higher-order dissipation is only activated at the beginning of the second plastic stage, reducing the hardening slope.

Concerning the non-proportional loading conditions, two cases are considered (Fig. 13). In the first case (one-side non-proportional loading), non-proportional passivation is only applied on the top edge of the studied strip, while the bottom edge is passivated over the entire simulation. This case allows plastic slip gradients to develop before activation of the non-proportional loading source. The associated comparison results are given in Fig. 13a. The Gurtin-type model leads to elastic gaps at both the initial yield and the occurrence of the non-proportional loading source. The occurrence of the latter source interrupts of the already initiated plastic flow until the mechanical state (evolving elastically) reaches a new yield point. This phenomenon, which is widely encountered using Gurtin-type gradient models including higher-order dissipation, is largely questioned in the literature. Indeed, it reflects a finite change in the higher-order stresses after an infinitesimal change in the plastic slip gradients. As shown in Fig. 13a, such a phenomenon is not encountered using the present model, which predicts no elastic gaps neither at the initial yield nor at the occurrence of the non-proportional loading source. This can be confirmed by the results of the second non-proportional loading case (two-edge non-proportional loading), where non-proportional passivation is

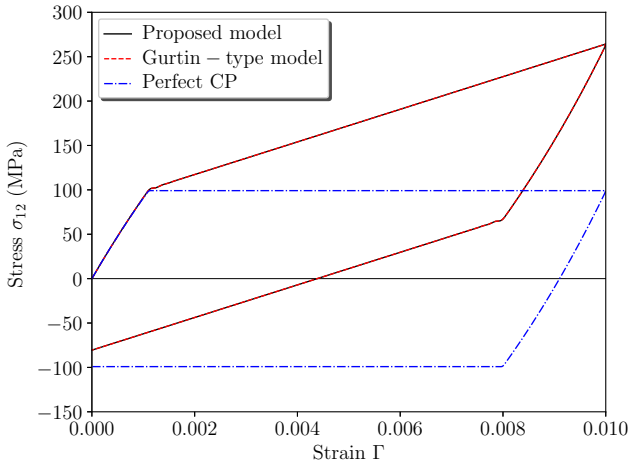

(a) Absence of higher-order dissipation ($l_d/h = 0$).

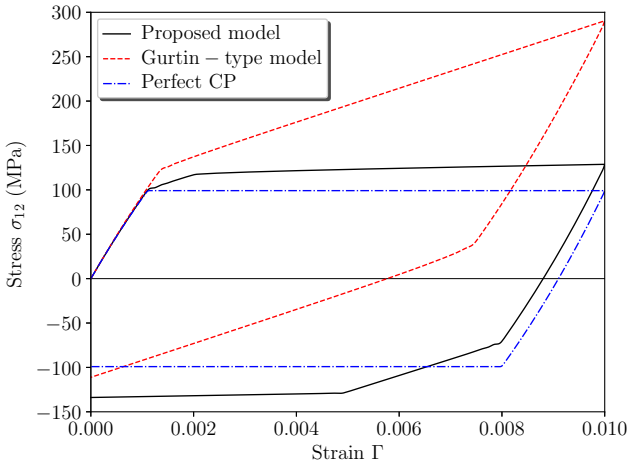

(b) Presence of higher-order dissipation ($l_d/h = 0.5$).

Fig. 12. Comparison between the present model and the Gurtin-type model of Jebahi et al. (2020) using proportional shear loading conditions ($n = 2$, $l_{en}/h = 5$, $S_{\xi 0} = 10\,\text{MPa}$, $H_\xi = 100\,\text{MPa}$).

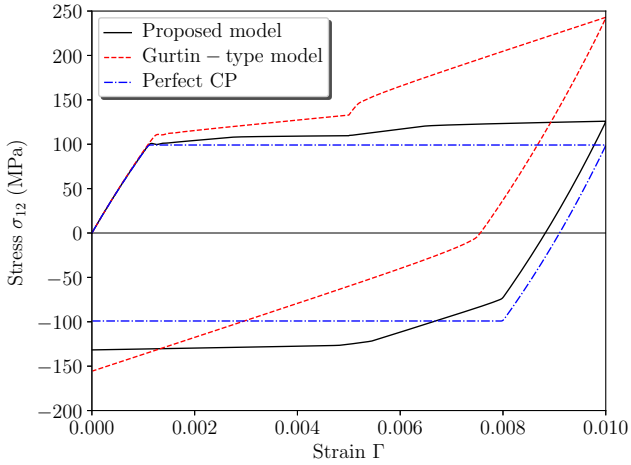

(a) One-side non-proportional shear loading.

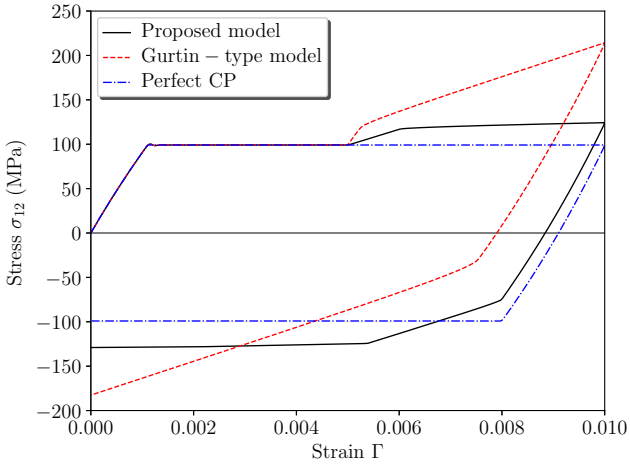

(b) Two-side non-proportional shear loading.

Fig. 13. Comparison between the present model and the Gurtin-type model of Jebahi et al. (2020) using non-proportional shear loading conditions ($n = 2$, $l_{en}/h = 5$, $l_d/h = 0.5$, $S_{\xi 0} = 10\,\text{MPa}$, $H_\xi = 100\,\text{MPa}$).

applied on both the top and bottom edges (Fig. 13b). Although no plastic slip gradients develop during the first loading stage (prior to the activation of the non-proportional loading source), this case is characterized by higher plastic slip gradients at the second loading stage, allowing for a better investigation of the formation of elastic gaps. In the absence of plastic slip gradients, the two models are equivalent and behave as classical crystal plasticity model. At the occurrence of the non-proportional loading source, contrary to the Gurtin-type model which leads to an elastic gap, the present model only predicts an increase in the plastic slope, with no plastic interruption (Fig. 13b).

In the context of classical Gurtin-type models, which are based on higher-order stress decomposition, the occurrence of elastic gaps under certain loading conditions is due to the presence of higher-order dissipative stresses. To satisfy the requirement of non-negative dissipation, these stresses are generally directly expressed in terms of plastic slip gradient rates. As a consequence, an infinitesimal change in the plastic slip gradients can sometimes cause a finite change in these stresses, leading to an abrupt increase of the generalized yield surface and then to the formation of elastic gaps. Almost all existing classical Gurtin-type models including higher-order dissipation lead to elastic gaps for some boundary value problems (Fleck et al., 2015). In the present work, which is based on plastic slip gradient decomposition, the higher-order dissipation is accounted for through the dissipative plastic slip gradient parts, while the higher-order stresses are taken as purely recoverable. This allows for avoiding the phenomenon of elastic gaps (when required), while considering thermodynamically-consistent higher-order dissipation.

5. Conclusion

A strain gradient crystal plasticity (SGCP) model has been developed in the present paper, based on an alternative description of the recoverable and dissipative higher-order effects. Instead of using the classical higher-order stress decomposition, which is widely used in Gurtin-type gradient-enhanced models, kinematic decomposition of the plastic slip gradients into recoverable and dissipative parts has been proposed to describe these effects. Although briefly discussed in some gradient-enhanced works (de Borst, 1993; Gologanu et al., 1997; Forest et al., 1997; Fleck and Hutchinson, 1997; Forest and Sievert, 2003; Forest, 2009), no in-depth investigation of this decomposition technique exists in the literature, particularly in the context of SGCP. The present work is complementary to that proposed by Panteghini et al. (2019) using multiple kinematic decomposition in the context of phenomenological gradient-based theories. To study the effects of the proposed kinematic decomposition on the response of materials, a simplified two-dimensional (2D) version of the developed SGCP model has been implemented within Abaqus/Standard, using a User-ELement (UEL) subroutine. The implementation has been performed assuming generalized non-quadratic defect energy and rate-dependent framework. The implemented version has been applied to simulate classical simple shear tests under proportional and non-proportional loading conditions.

The case of quadratic defect energy has first been considered to better investigate the effects of the proposed kinematic decomposition, in the absence of complex nonlinear hardening phenomena. Using non-zero dissipative length scale l_d and initial higher-order dissipative slip resistance $S_{\xi 0}$, two-stage plastic behavior is obtained after the initial yielding. First, relatively steep-sloped plastic evolution appears beyond the classical crystal plasticity (CP) yield stress. Then, a significant decrease in the plastic slope is observed at a further higher-order yield stress, corresponding to activation of the higher-order dissipation. This idealized two-stage plastic behavior is due to the simplicity of the considered 2D shear sample with only two symmetric planar slip systems. The observed higher-order yield stress can be interpreted as an apparent yield stress and is controlled by l_d and $S_{\xi 0}$. It has been shown that this yield stress increases linearly with the reciprocal of the studied strip thickness ($\propto h^{-1}$), which corresponds to the well-known Orowan relation. The obtained h^{-1} scaling law also complies with recent experimental investigations of size effects showing that the size dependence exponent could vary between -1 and -0.5 (De Sansal et al., 2010; Cordero et al., 2016; Jiang et al., 2019), or also between -1 and -0.2 (Dunstan and Bushby, 2014). Using very small $S_{\xi 0}$ (with

non-zero l_d and H_ξ), the higher-order yield stress converges towards the initial yield stress (corresponding to classical CP). In this case, one-stage plasticity is obtained with the hardening behavior simultaneously controlled by the recoverable and dissipative higher-order effects. The latter effects lead to classical dissipative (isotropic-like) hardening, whose slope can be controlled by both the dissipative length scale l_d and the higher-order hardening parameter H_ξ.

Introducing the case of non-quadratic defect energy, it is known that this case yields complex nonlinear kinematic hardening behavior with inflection points under reverse loading. Effects of the proposed kinematic decomposition on this behavior have been investigated using less-than-two values of the defect energy index n. Results of this investigation have brought to light interesting features of the higher-order dissipation. Activation of the higher-order dissipative effects reduces the width of the inflection region under reverse loading. Using an appropriate choice of l_d and $S_{\xi 0}$ with small defect energy index n (*i.e.,* close to 1), even if clear strengthening effects take place at the initial yield, the inflection phenomenon occurs in a very narrow (invisible) region, with no unusual effects on the dissipative (isotropic-like) hardening behavior beyond the apparent (higher-order) yielding. This provides a way for the proposed SGCP model to simulate strengthening effects, which are confirmed experimentally, while obtaining nearly classical hardening behavior at the macroscopic scale.

Comparison between results of the proposed SGCP model and the Gurtin-type model of Jebahi et al. (2020), which is based on classical higher-order stress decomposition, under proportional and non-proportional loading conditions, shows that the present model allows for avoiding elastic gaps for any boundary conditions, even when considering higher-order dissipation. It is worth mentioning that only the recent phenomenological SGP model of Panteghini et al. (2019) is capable of considering thermodynamically-consistent higher-order dissipation while systematically avoiding elastic gaps. In the context of gradient-enhanced crystal plasticity, no model providing such capabilities exists in the literature, except for the one proposed in the present work. Note that the authors' attitude on the real existence of these gaps is rather agnostic. This question will be investigated in further work based in particular on specific experimental results. Although yielding no elastic gaps, the proposed model can predict strengthening-like phenomena thanks to the competition between the recoverable and dissipative higher-order effects.

Acknowledgments

The authors acknowledge the financial support of the French National Research Agency (ANR) under reference ANR-20-CE08-0010 (SGP-GAPS project).

Appendix A. Higher-order stresses

Appendix A.1. Computation of $\boldsymbol{\xi}^\alpha$

The free energy density used in this work is given by:

$$\psi\left(\boldsymbol{\varepsilon}_e,\, \boldsymbol{\kappa}_r\right) = \frac{1}{2}\,\boldsymbol{\varepsilon}_e : \mathbf{C} : \boldsymbol{\varepsilon}_e + \frac{1}{n}\,X_0\,l_{en}^n \sum_{\alpha=1}^{q} \left[\left|\mathbf{s}^\alpha \cdot \boldsymbol{\kappa}_r^\alpha\right|^n + \left|\mathbf{l}^\alpha \cdot \boldsymbol{\kappa}_r^\alpha\right|^n\right] \tag{A.1}$$

The higher-order microscopic stress associated with slip system α, which is assumed to be purely recoverable, can be deduced from ψ as follows:

$$\begin{aligned}\boldsymbol{\xi}^{\alpha} &= \frac{\partial \psi}{\partial \boldsymbol{\kappa}_r^{\alpha}} \\ &= X_0\, l_{en}^n \left[|\mathbf{s}^{\alpha} \cdot \boldsymbol{\kappa}_r^{\alpha}|^{n-1} \, \frac{\partial \left| \mathbf{s}^{\alpha} \cdot \boldsymbol{\kappa}_r^{\alpha} \right|}{\partial \boldsymbol{\kappa}_r^{\alpha}} + |\mathbf{l}^{\alpha} \cdot \boldsymbol{\kappa}_r^{\alpha}|^{n-1} \, \frac{\partial \left| \mathbf{l}^{\alpha} \cdot \boldsymbol{\kappa}_r^{\alpha} \right|}{\partial \boldsymbol{\kappa}_r^{\alpha}} \right]\end{aligned} \tag{A.2}$$

The partial derivative terms in the above expression can be calculated as:

$$\begin{aligned}\frac{\partial \left| \mathbf{s}^{\alpha} \cdot \boldsymbol{\kappa}_r^{\alpha} \right|}{\partial \boldsymbol{\kappa}_r^{\alpha}} &= \frac{\partial \sqrt{\left(\mathbf{s}^{\alpha} \cdot \boldsymbol{\kappa}_r^{\alpha} \right)^2}}{\partial \boldsymbol{\kappa}_r^{\alpha}} \\ &= \frac{1}{2\sqrt{\left(\mathbf{s}^{\alpha} \cdot \boldsymbol{\kappa}_r^{\alpha} \right)^2}} \frac{\partial \left(\mathbf{s}^{\alpha} \cdot \boldsymbol{\kappa}_r^{\alpha} \right)^2}{\partial \boldsymbol{\kappa}_r^{\alpha}} \\ &= \frac{\mathbf{s}^{\alpha} \cdot \boldsymbol{\kappa}_r^{\alpha}}{\sqrt{\left(\mathbf{s}^{\alpha} \cdot \boldsymbol{\kappa}_r^{\alpha} \right)^2}} \frac{\partial \left(\mathbf{s}^{\alpha} \cdot \boldsymbol{\kappa}_r^{\alpha} \right)}{\partial \boldsymbol{\kappa}_r^{\alpha}} \\ &= \frac{\mathbf{s}^{\alpha} \cdot \boldsymbol{\kappa}_r^{\alpha}}{\sqrt{\left(\mathbf{s}^{\alpha} \cdot \boldsymbol{\kappa}_r^{\alpha} \right)^2}} \mathbf{s}^{\alpha} \\ &= \frac{\mathbf{s}^{\alpha} \otimes \mathbf{s}^{\alpha}}{\left| \mathbf{s}^{\alpha} \cdot \boldsymbol{\kappa}_r^{\alpha} \right|} \cdot \boldsymbol{\kappa}_r^{\alpha}\end{aligned} \tag{A.3}$$

and:

$$\frac{\partial \left| \mathbf{l}^{\alpha} \cdot \boldsymbol{\kappa}_r^{\alpha} \right|}{\partial \boldsymbol{\kappa}_r^{\alpha}} = \frac{\mathbf{l}^{\alpha} \otimes \mathbf{l}^{\alpha}}{\left| \mathbf{l}^{\alpha} \cdot \boldsymbol{\kappa}_r^{\alpha} \right|} \cdot \boldsymbol{\kappa}_r^{\alpha} \tag{A.4}$$

which leads to:

$$\boldsymbol{\xi}^{\alpha} = X_0\, l_{en}^n \left[|\mathbf{s}^{\alpha} \cdot \boldsymbol{\kappa}_r^{\alpha}|^{n-2} \, \mathbf{s}^{\alpha} \otimes \mathbf{s}^{\alpha} + |\mathbf{l}^{\alpha} \cdot \boldsymbol{\kappa}_r^{\alpha}|^{n-2} \, \mathbf{l}^{\alpha} \otimes \mathbf{l}^{\alpha} \right] \cdot \boldsymbol{\kappa}_r^{\alpha} \tag{A.5}$$

Appendix A.2. Computation of $\dot{\boldsymbol{\xi}}^{\alpha}$

The rate of the higher-order stress associated with slip system α can be calculated as follows:

$$\dot{\boldsymbol{\xi}}^{\alpha} = \frac{\partial \boldsymbol{\xi}^{\alpha}}{\partial \boldsymbol{\kappa}_r^{\alpha}} \cdot \dot{\boldsymbol{\kappa}}_r^{\alpha} \tag{A.6}$$

The partial derivative of $\boldsymbol{\xi}^{\alpha}$ with respect of $\boldsymbol{\kappa}_r^{\alpha}$ can be calculated as:

$$\begin{aligned}\frac{\partial \boldsymbol{\xi}^{\alpha}}{\partial \boldsymbol{\kappa}_r^{\alpha}} &= \frac{\partial}{\partial \boldsymbol{\kappa}_r^{\alpha}} \left(X_0\, l_{en}^n \left[|\mathbf{s}^{\alpha} \cdot \boldsymbol{\kappa}_r^{\alpha}|^{n-2} \, \mathbf{s}^{\alpha} \otimes \mathbf{s}^{\alpha} + |\mathbf{l}^{\alpha} \cdot \boldsymbol{\kappa}_r^{\alpha}|^{n-2} \, \mathbf{l}^{\alpha} \otimes \mathbf{l}^{\alpha} \right] \cdot \boldsymbol{\kappa}_r^{\alpha} \right) \\ &= \frac{\partial}{\partial \boldsymbol{\kappa}_r^{\alpha}} \left(X_0\, l_{en}^n \, |\mathbf{s}^{\alpha} \cdot \boldsymbol{\kappa}_r^{\alpha}|^{n-2} \left[\mathbf{s}^{\alpha} \otimes \mathbf{s}^{\alpha} \cdot \boldsymbol{\kappa}_r^{\alpha} \right] \right) + \frac{\partial}{\partial \boldsymbol{\kappa}_r^{\alpha}} \left(X_0\, l_{en}^n \, |\mathbf{l}^{\alpha} \cdot \boldsymbol{\kappa}_r^{\alpha}|^{n-2} \left[\mathbf{l}^{\alpha} \otimes \mathbf{l}^{\alpha} \cdot \boldsymbol{\kappa}_r^{\alpha} \right] \right)\end{aligned} \tag{A.7}$$

with:

$$\begin{aligned}\frac{\partial}{\partial \boldsymbol{\kappa}_r^\alpha}\left(X_0\, l_{en}^n\, |\mathbf{s}^\alpha \cdot \boldsymbol{\kappa}_r^\alpha|^{n-2}\, [\,\mathbf{s}^\alpha \otimes \mathbf{s}^\alpha \cdot \boldsymbol{\kappa}_r^\alpha]\right) &= (n-2)\; X_0\, l_{en}^n\, |\mathbf{s}^\alpha \cdot \boldsymbol{\kappa}_r^\alpha|^{n-3}\, \frac{[\mathbf{s}^\alpha \otimes \mathbf{s}^\alpha \cdot \boldsymbol{\kappa}_r^\alpha]}{|\mathbf{s}^\alpha \cdot \boldsymbol{\kappa}_r^\alpha|} \otimes [\,\mathbf{s}^\alpha \otimes \mathbf{s}^\alpha \cdot \boldsymbol{\kappa}_r^\alpha] \\ &\quad + X_0\, l_{en}^n\, |\mathbf{s}^\alpha \cdot \boldsymbol{\kappa}_r^\alpha|^{n-2}\, \mathbf{s}^\alpha \otimes \mathbf{s}^\alpha \\ &= (n-2)\; X_0\, l_{en}^n\, |\mathbf{s}^\alpha \cdot \boldsymbol{\kappa}_r^\alpha|^{n-3}\, \frac{(\mathbf{s}^\alpha \cdot \boldsymbol{\kappa}_r^\alpha)^2}{|\mathbf{s}^\alpha \cdot \boldsymbol{\kappa}_r^\alpha|}\, \mathbf{s}^\alpha \otimes \mathbf{s}^\alpha \\ &\quad + X_0\, l_{en}^n\, |\mathbf{s}^\alpha \cdot \boldsymbol{\kappa}_r^\alpha|^{n-2}\, \mathbf{s}^\alpha \otimes \mathbf{s}^\alpha \\ &= (n-1)\; X_0\, l_{en}^n\, |\mathbf{s}^\alpha \cdot \boldsymbol{\kappa}_r^\alpha|^{n-2}\, \mathbf{s}^\alpha \otimes \mathbf{s}^\alpha\end{aligned} \tag{A.8}$$

and:

$$\frac{\partial}{\partial \boldsymbol{\kappa}_r^\alpha}\left(X_0\, l_{en}^n\, |\mathbf{l}^\alpha \cdot \boldsymbol{\kappa}_r^\alpha|^{n-2}\, [\,\mathbf{l}^\alpha \otimes \mathbf{l}^\alpha \cdot \boldsymbol{\kappa}_r^\alpha]\right) = (n-1)\; X_0\, l_{en}^n\, |\mathbf{l}^\alpha \cdot \boldsymbol{\kappa}_r^\alpha|^{n-2}\, \mathbf{l}^\alpha \otimes \mathbf{l}^\alpha \tag{A.9}$$

Therefore,

$$\begin{aligned}\frac{\partial \boldsymbol{\xi}^\alpha}{\partial \boldsymbol{\kappa}_r^\alpha} &= (n-1)\, X_0\, l_{en}^n\, \left[|\mathbf{s}^\alpha \cdot \boldsymbol{\kappa}_r^\alpha|^{n-2}\, \mathbf{s}^\alpha \otimes \mathbf{s}^\alpha + |\mathbf{l}^\alpha \cdot \boldsymbol{\kappa}_r^\alpha|^{n-2}\, \mathbf{l}^\alpha \otimes \mathbf{l}^\alpha\right] \\ &= \mathbf{A}^{\alpha\alpha}\end{aligned} \tag{A.10}$$

and:

$$\dot{\boldsymbol{\xi}}^\alpha = \mathbf{A}^{\alpha\alpha} \cdot \dot{\boldsymbol{\kappa}}_r^\alpha \tag{A.11}$$

Appendix A.3. Computation of $\boldsymbol{\nabla} \cdot \boldsymbol{\xi}^\alpha$

The higher-order stress associated with slip system α, $\boldsymbol{\xi}^\alpha$, is only a function of $\boldsymbol{\kappa}_r^\alpha$. Following the same derivation steps as in Appendix A.2, the divergence of $\boldsymbol{\xi}^\alpha$ can then be calculated as:

$$\begin{aligned}\boldsymbol{\nabla} \cdot \boldsymbol{\xi}^\alpha &= \frac{\partial \boldsymbol{\xi}^\alpha}{\partial \boldsymbol{\kappa}_r^\alpha} : [\boldsymbol{\nabla} \boldsymbol{\kappa}_r^\alpha]^T \\ &= \mathbf{A}^{\alpha\alpha} : \boldsymbol{\nabla} \boldsymbol{\kappa}_r^\alpha\end{aligned} \tag{A.12}$$

$\mathbf{A}^{\alpha\alpha}$ is symmetric tensor given by (A.10).

References

Acharya, A., Bassani, J.L., 2000. Lattice incompatibility and a gradient theory of crystal plasticity. J. Mech. Phys. Solids 48, 1565–1595.

Aifantis, E.C., 1984. On the microstructural origin of certain inelastic models. J. Eng. Mater. Technol. 106, 326.

Aifantis, E.C., 1987. The physics of plastic deformation. Int. J. Plast. 3, 211–247.

Aifantis, E.C., 1999. Strain gradient interpretation of size effects. Int. J. Fract. 95, 299–314.

Anand, L., Aslan, O., Chester, S.A., 2012. A large-deformation gradient theory for elastic-plastic materials: Strain softening and regularization of shear bands. Int. J. Plast. 30-31, 116–143.

Arsenlis, A., Parks, D.M., 1999. Crystallographic aspects of geometrically-necessary and statistically-stored dislocation density. Acta Mater. 47, 1597–1611.

Asaro, R.J., 1975. Elastic-plastic memory and kinematic-type hardening. Acta Metall. 23, 1255–1265.

Ashby, M.F., 1970. The deformation of plastically non-homogeneous materials. Philos. Mag. 21, 399–424.

Bardella, L., 2010. Size effects in phenomenological strain gradient plasticity constitutively involving the plastic spin. Int. J. Eng. Sci. 48, 550–568.

Bardella, L., 2021. On a mixed energetic-dissipative contitutive law for non-proportional loading, with focus on small-scale plasticity. Proc. R. Soc. A Math. Phys. Eng. Sci. 477, rspa.2020.0940.

Bardella, L., Panteghini, A., 2015. Modelling the torsion of thin metal wires by distortion gradient plasticity. J. Mech. Phys. Solids 78, 467–492.

Bayerschen, E., Böhlke, T., 2016. Power-law defect energy in a single-crystal gradient plasticity framework: a computational study. Comput. Mech. 58, 13–27.

de Borst, R., 1993. A generalisation of J2-flow theory for polar continua. Comput. Methods Appl. Mech. Eng. 103, 347–362.

Cai, L., Jebahi, M., Abed-Meraim, F., 2021. Strain Localization Modes within Single Crystals Using Finite Deformation Strain Gradient Crystal Plasticity. Crystals 11, 1235.

Cordero, N.M., Gaubert, A., Forest, S., Busso, E.P., Gallerneau, F., Kruch, S., 2010. Size effects in generalised continuum crystal plasticity for two-phase laminates. J. Mech. Phys. Solids 58, 1963–1994.

Cordero, Z.C., Knight, B.E., Schuh, C.A., 2016. Six decades of the Hall-Petch effect - a survey of grain-size strengthening studies on pure metals. Int. Mater. Rev. 61, 495–512.

Dahlberg, C.F.O., Saito, Y., Öztop, M.S., Kysar, J.W., 2017. Geometrically necessary dislocation density measurements at a grain boundary due to wedge indentation into an aluminum bicrystal. J. Mech. Phys. Solids 105, 131–149.

De Sansal, C., Devincre, B., Kubin, L., 2010. Grain size strengthening in microcrystalline copper: A three-dimensional dislocation dynamics simulation. Key Eng. Mater. 423, 25–32.

Dunstan, D.J., Bushby, A.J., 2014. Grain size dependence of the strength of metals: The Hall-Petch effect does not scale as the inverse square root of grain size. Int. J. Plast. 53, 56–65.

El-Naaman, S.A., Nielsen, K.L., Niordson, C.F., 2019. An investigation of back stress formulations under cyclic loading. Mech. Mater. 130, 76–87.

Fleck, N.A., Hutchinson, J.W., 1997. Strain Gradient Plasticity. Adv. Appl. Mech. 33, 295–361.

Fleck, N.A., Hutchinson, J.W., 2001. A reformulation of strain gradient plasticity. J. Mech. Phys. Solids 49, 2245–2271.

Fleck, N.A., Hutchinson, J.W., Willis, J.R., 2014. Strain gradient plasticity under non-proportional loading. Proc. R. Soc. A Math. Phys. Eng. Sci. 470, 0267.

Fleck, N.A., Hutchinson, J.W., Willis, J.R., 2015. Guidelines for constructing strain gradient plasticity theories. J. Appl. Mech. 82, 071002.

Fleck, N.A., Muller, G.M., Ashby, M.F., Hutchinson, J.W., 1994. Strain gradient plasticity: Theory and experiment. Acta Metall. Mater. 42, 475–487.

Fleck, N.A., Willis, J.R., 2009. A mathematical basis for strain-gradient plasticity theory. Part I: Scalar plastic multiplier. J. Mech. Phys. Solids 57, 161–177.

Forest, S., 2009. Micromorphic Approach for Gradient Elasticity, Viscoplasticity, and Damage. J. Eng. Mech. 135, 117–131.

Forest, S., 2020. Continuum thermomechanics of nonlinear micromorphic, strain and stress gradient media. Philos. Trans. Royal Soc. A 378, 20190169.

Forest, S., Aifantis, E.C., 2010. Some links between recent gradient thermo-elasto-plasticity theories and the thermomechanics of generalized continua. Int. J. Solids Struct. 47, 3367–3376.

Forest, S., Bertram, A., 2011. Formulations of Strain Gradient Plasticity, in: Mechanics of generalized continua. volume 53, pp. 137–149.

Forest, S., Cailletaud, G., Sievert, R., 1997. A Cosserat theory for elastoviscoplastic single crystals at finite deformation. Arch. Mech. 49, 705–736.

Forest, S., Guéninchault, N., 2013. Inspection of free energy functions in gradient crystal plasticity. Acta Mech. Sin. Xuebao 29, 763–772.

Forest, S., Mayeur, J.R., McDowell, D.L., 2019. Micromorphic crystal plasticity, in: Handb. Nonlocal Contin. Mech. Mater. Struct.. Springer International Publishing, Cham, pp. 643–686.

Forest, S., Sievert, R., 2003. Elastoviscoplastic constitutive frameworks for generalized continua. Acta Mech. 160, 71–111.

Germain, P., 1973. The method of virtual power in continuum mechanics. Part 2: Microstructure. SIAM J. Appl. Math. 25, 556–575.

Gologanu, M., Leblond, J., Devaux, J., 1997. Continuum micromechanics. Springer Verlag, CISM Courses and Lectures No. 377. volume 377. chapter Recent extensions of Gurson's model for porous ductile metals. pp. 61–130.

Gudmundson, P., 2004. A unified treatment of strain gradient plasticity. J. Mech. Phys. Solids 52, 1379–1406.

Gurtin, M.E., 2002. A gradient theory of single-crystal viscoplasticity that accounts for geometrically necessary dislocations. J. Mech. Phys. Solids 50, 5–32.

Gurtin, M.E., 2004. A gradient theory of small-deformation isotropic plasticity that accounts for the Burgers vector and for dissipation due to plastic spin. J. Mech. Phys. Solids 52, 2545–2568.

Gurtin, M.E., 2008. A finite-deformation, gradient theory of single-crystal plasticity with free energy dependent on densities of geometrically necessary dislocations. Int. J. Plast. 24, 702–725.

Gurtin, M.E., Anand, L., 2009. Thermodynamics applied to gradient theories involving the accumulated plastic strain: The theories of Aifantis and Fleck and Hutchinson and their generalization. J. Mech. Phys. Solids 57, 405–421.

Gurtin, M.E., Anand, L., Lele, S.P., 2007. Gradient single-crystal plasticity with free energy dependent on dislocation densities. J. Mech. Phys. Solids 55, 1853–1878.

Gurtin, M.E., Fried, E., Anand, L., 2010. The Mechanics and Thermodynamics of Continua. Cambridge University Press, New York.

Hutchinson, J.W., 2012. Generalizing J 2 flow theory: Fundamental issues in strain gradient plasticity. Acta Mech. Sin. 28, 1078–1086.

Jebahi, M., Cai, L., Abed-Meraim, F., 2020. Strain gradient crystal plasticity model based on generalized non-quadratic defect energy and uncoupled dissipation. Int. J. Plast. 126, 102617.

Jebahi, M., Forest, S., 2021. Scalar-based strain gradient plasticity theory to model size-dependent kinematic hardening effects. Contin. Mech. Thermodyn. 33, 1223–1245.

Jiang, M., Devincre, B., Monnet, G., 2019. Effects of the grain size and shape on the flow stress: A dislocation dynamics study. Int. J. Plast. 113, 111–124.

Liu, D., He, Y., Dunstan, D.J., Zhang, B., Gan, Z., Hu, P., Ding, H., 2013. Anomalous plasticity in the cyclic torsion of micron scale metallic wires. Phys. Rev. Lett. 110, 244301.

Ma, Z.S., Zhou, Y.C., Long, S.G., Lu, C., 2012. On the intrinsic hardness of a metallic film/substrate system: Indentation size and substrate effects. Int. J. Plast. 34, 1–11.

Martínez-Pañeda, E., Deshpande, V.S., Niordson, C.F., Fleck, N.A., 2019. The role of plastic strain gradients in the crack growth resistance of metals. J. Mech. Phys. Solids 126, 136–150.

Mühlhaus, H.B., Alfantis, E.C., 1991. A variational principle for gradient plasticity. Int. J. Solids Struct. 28, 845–857.

Nellemann, C., Niordson, C.F., Nielsen, K.L., 2017. An incremental flow theory for crystal plasticity incorporating strain gradient effects. Int. J. Solids Struct. 110-111, 239–250.

Nellemann, C., Niordson, C.F., Nielsen, K.L., 2018. Hardening and strengthening behavior in rate-independent strain gradient crystal plasticity. Eur. J. Mech. A/Solids , 157–168.

Niordson, C.F., Hutchinson, J.W., 2003. On lower order strain gradient plasticity theories. Eur. J. Mech. A/Solids 22, 771–778.

Nye, J.F., 1953. Some geometrical relations in dislocated crystals. Acta Metall. 1, 153–162.

Ohno, N., Okumura, D., 2007. Higher-order stress and grain size effects due to self-energy of geometrically necessary dislocations. J. Mech. Phys. Solids 55, 1879–1898.

Panteghini, A., Bardella, L., 2016. On the Finite Element implementation of higher-order gradient plasticity, with focus on theories based on plastic distortion incompatibility. Comput. Methods Appl. Mech. Eng. 310, 840–865.

Panteghini, A., Bardella, L., 2018. On the role of higher-order conditions in distortion gradient plasticity. J. Mech. Phys. Solids 118, 293–321.

Panteghini, A., Bardella, L., 2020. Modelling the cyclic torsion of polycrystalline micron-sized copper wires by distortion gradient plasticity. Philos. Mag. 100, 2352–2364.

Panteghini, A., Bardella, L., Niordson, C.F., 2019. A potential for higher-order phenomenological strain gradient plasticity to predict reliable response under non-proportional loading. Proc. R. Soc. A 475, 20190258.

Regueiro, R.A., 2010. On finite strain micromorphic elastoplasticity. Int. J. Solids Struct. 47, 786–800.

Sarac, A., Oztop, M.S., Dahlberg, C.F.O., Kysar, J.W., 2016. Spatial distribution of the net burgers vector density in a deformed single crystal. Int. J. Plast. 85, 110–129.

Šilhavý, M., 1997. The Mechanics and Thermodynamics of Continuous Media. Springer Berlin Heidelberg, Berlin, Heidelberg.

Svendsen, B., Bargmann, S., 2010. On the continuum thermodynamic rate variational formulation of models for extended crystal plasticity at large deformation. J. Mech. Phys. Solids 58, 1253–1271.

Voyiadjis, G.Z., Deliktas, B., 2009. Mechanics of strain gradient plasticity with particular reference to decomposition of the state variables into energetic and dissipative components. Int. J. Eng. Sci. 47, 1405–1423.

Voyiadjis, G.Z., Song, Y., 2019. Strain gradient continuum plasticity theories: Theoretical, numerical and experimental investigations. Int. J. Plast. 121, 21–75.

Voyiadjis, G.Z., Song, Y., 2020. Review of theoretical developments on the gradient-enhanced continuum plasticity, in: Gradient-Enhanced Continuum Plasticity. Elsevier, pp. 43–93.

Wulfinghoff, S., Böhlke, T., 2015. Gradient crystal plasticity including dislocation-based work-hardening and dislocation transport. Int. J. Plast. 69, 152–169.

Wulfinghoff, S., Forest, S., Böhlke, T., 2015. Strain gradient plasticity modeling of the cyclic behavior of laminate microstructures. J. Mech. Phys. Solids 79, 1–20.

Yalçinkaya, T., 2016. Strain Gradient Crystal Plasticity: Thermodynamics and Implementation, in: Voyiadjis, G.Z. (Ed.), Handbook of Nonlocal Continuum Mechanics for Materials and Structures. Springer International Publishing, Cham, pp. 1–32.